

# Dual-Polarization Radar Data Analysis of the Impact of Ground-Based Glaciogenic Seeding on Winter Orographic Clouds. Part I: Mostly Stratiform Clouds

XIAOQIN JING AND BART GEERTS

*Department of Atmospheric Science, University of Wyoming, Laramie, Wyoming*

KATJA FRIEDRICH

*Department of Atmospheric and Oceanic Sciences, University of Colorado Boulder, Boulder, Colorado*

BINOD POKHAREL

*Department of Atmospheric Science, University of Wyoming, Laramie, Wyoming*

(Manuscript received 29 September 2014, in final form 12 May 2015)

## ABSTRACT

The impact of ground-based glaciogenic seeding on wintertime orographic, mostly stratiform clouds is analyzed by means of data from an X-band dual-polarization radar, the Doppler-on-Wheels (DOW) radar, positioned on a mountain pass. This study focuses on six intensive observation periods (IOPs) during the 2012 AgI Seeding Cloud Impact Investigation (ASCII) project in Wyoming. In all six storms, the bulk upstream Froude number below mountaintop exceeded 1 (suggesting unblocked flow), the clouds were relatively shallow (with bases below freezing), some liquid water was present, and orographic flow conditions were mostly steady. To examine the silver iodide (AgI) seeding effect, three study areas are defined (a control area, a target area upwind of the crest, and a lee target area), and comparisons are made between measurements from a treated period and those from an untreated period. Changes in reflectivity and differential reflectivity observed by the DOW at low levels during seeding are consistent with enhanced snow growth, by vapor diffusion and/or aggregation, for a case study and for the composite analysis of all six IOPs, especially at close range upwind of the mountain crest. These low-level changes may have been affected by natural changes aloft, however, as evident from differences in the evolution of the echo-top height in the control and target areas. Even though precipitation in the target region is strongly correlated with that in the control region, the authors cannot definitively attribute the change to seeding because there is a lack of knowledge about natural variability, nor can the outcome be generalized, because the sample size is small.

## 1. Introduction

In an effort to enhance precipitation, especially in arid regions, glaciogenic cloud seeding has been conducted since the 1940s (e.g., [Smith 1949](#); [Langmuir 1950](#); [Vonnegut and Chessin 1971](#); [Hobbs et al. 1981](#); [Bruintjes 1999](#)). Silver iodide (AgI) has been widely used in both ground-based and airborne seeding because it has a crystal structure that is similar to that of ice ([Vonnegut and Chessin 1971](#)) and therefore AgI particles can act as

ice nuclei at temperatures higher than can most natural aerosol ([DeMott 1997](#)). In the case of cloud seeding, the main precipitation-enhancement mechanism in cold-season orographic clouds is believed to be *static* ([Bruintjes 1999](#)); that is, the increased number of ice nuclei at a given temperature allows more efficient transformation of supercooled water to snow during orographic ascent, by vapor diffusion and/or droplet accretion ([Gagin 1986](#)). Under moist-neutral or less-stable conditions, the orographic flow itself may be altered as air parcels gain buoyancy because of the extra latent heat release as liquid water freezes in the seeded cloud, resulting in deeper convective clouds (*dynamic* seeding; [Simpson and Woodley 1971](#); [Rosenfeld and Woodley 1989](#)).

---

*Corresponding author address:* Xiaoqin Jing, Dept. of Atmospheric Science, University of Wyoming, 1000 E. University Ave., Laramie, WY 82071.  
E-mail: xjing@uwyo.edu

The effectiveness of cloud seeding in enhancing orographic precipitation remains uncertain, and optimal seeding conditions remain poorly understood (Bruitjes 1999; Silverman 2001). Several studies have attempted to document the cloud microphysical “chain of events.” Some of these studies improved the understanding of AgI plume dispersal (Super 1974; Holroyd et al. 1988; Boe et al. 2014; Xue et al. 2014). Others detailed the microphysical changes within these plumes as they disperse in the clouds (Super and Boe 1988; Super and Heimbach 1988; Deshler et al. 1990; Holroyd et al. 1995; Huggins 1995; Super 1999; Huggins 2007). Most of the cloud and precipitation studies examined individual cases rather than a population of storms. Their results emphasize the challenges in documenting changes in cloud microphysical processes related to AgI seeding. The National Research Council, in its 2003 report *Critical Issues in Weather Modification Research*, advocates further physical process studies in the context of seeding operations of opportunity, using state-of-the-art instruments and models (National Research Council 2003).

The study presented in this paper aims to do just that, mainly using data from a scanning X-band (3 cm) dual-polarization Doppler radar, deployed in the Sierra Madre in southern Wyoming as part of the 2012 AgI Seeding Cloud Impact Investigation (ASCII) campaign. This campaign was designed around ground-based AgI seeding opportunities under the Wyoming Weather Modification Pilot Project (WWMP; Breed et al. 2014).

Several papers have analyzed ASCII data, or pre-ASCII data collected over the same mountain ranges, and all involved ground-based seeding only. Geerts et al. (2010) uses flight-level and Wyoming Cloud Radar (WCR—an airborne profiling W-band Doppler radar) data to examine changes in the vertical profile of reflectivity. They find significant increases in radar reflectivity within the planetary boundary layer (PBL: 0.5–1 km deep) during cloud seeding relative to times without, but they do not compare target and control measurements. Miao and Geerts (2013) provide experimental evidence that AgI seeding can increase the number concentration and mixing ratio of ice crystals within the PBL. Pokharel et al. (2014a,b) examine a stratiform case and a shallow convective case, respectively, using data from an array of in situ and remote instruments on the ground and aboard an aircraft, in both a target area and a nearby control area. These case studies highlight the challenge of signal detection within the highly variable, finely textured fields of cloud and precipitation. They provide inconclusive but cumulative evidence for a seeding-induced increase in reflectivity and snow-crystal concentration, using the data from radars operating at different

frequencies and with different target and control regions, as well as from particle sizing and imaging probes on the ground and aboard an aircraft. Chu et al. (2014) evaluate the ability of the Weather Research and Forecasting (WRF) Model in large-eddy-simulation mode, with a point-source glaciogenic-seeding module, to reproduce the seeding impact observed in one case. They find an increase in low-level reflectivity during seeding in both the model and WCR observations in the target area, but only relative to changes between untreated and treated periods in the control area. Xue et al. (2015, manuscript submitted to *J. Appl. Meteor. Climatol.*) use the same case and modeling framework to describe AgI nuclei dispersal in clouds, mainly by buoyancy-induced eddies in this case, and to describe the enhanced ice initiation and snow growth in seeded clouds. In general, ground-based-seeding impact detection appears more challenging than airborne-seeding impact detection. The likely reasons for this are the turbulent nature of the near-surface flow and flow deflections by terrain, both of which increase the uncertainty of plume dispersal, and the possible natural introduction of small ice crystals into shallow orographic clouds from the ground up by wind gusts (Geerts et al. 2011; Vali et al. 2012).

Dual-polarization radar has been widely used to study precipitation systems. Several studies before ASCII have used radar data to assess glaciogenic-seeding impact (e.g., Simpson and Woodley 1971; Dennis et al. 1975; Gagin et al. 1986; Rosenfeld and Woodley 1989), including polarimetric radar data (Kucera et al. 2008), but most of these studies focused on warm-season convective clouds. A Doppler-on-Wheels (DOW) radar was deployed in ASCII at the Battle Pass (3 km MSL) in the Sierra Madre range in Wyoming (Fig. 1). The DOW used here measures the return signals at horizontal and vertical polarizations, yielding differential reflectivity ZDR, differential phase  $\Phi_{DP}$ , and correlation coefficient  $\rho_{HV}$ , in addition to Doppler velocity and reflectivity Z. We will use these products to study microphysical changes in clouds.

The objective of this study is to explore evidence for an impact of ground-based glaciogenic seeding on snow growth in orographic clouds using DOW data collected in ASCII. Here six mostly stratiform storms are analyzed. The experimental design and instrumentation are described in section 2. Section 3 presents the method used in this study. DOW data for one case study are discussed in section 4. A composite analysis of all six cases follows in section 5. A discussion follows in section 6, and conclusions are listed in section 7. In Jing and Geerts (2015), three cases with shallow convective precipitation are examined.

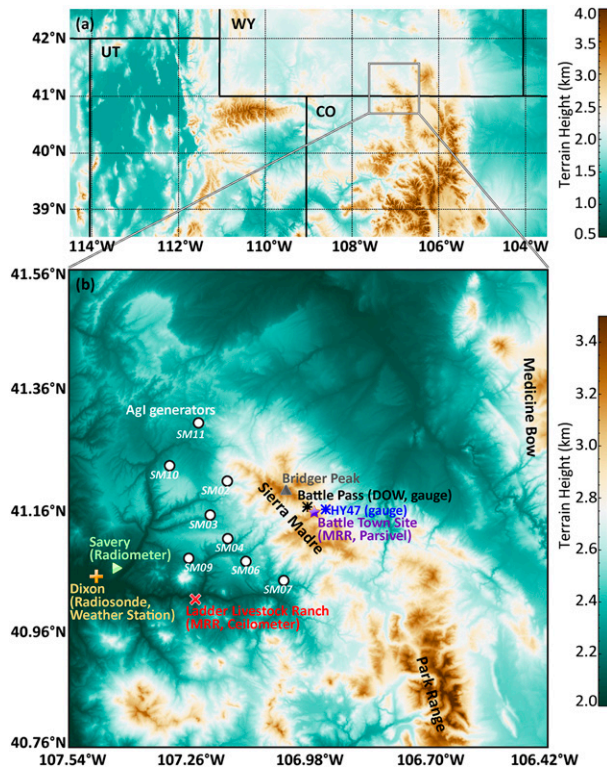


FIG. 1. ASCII-12 experimental design map. (a) The topography of the surrounding region, with a  $96 \times 96 \text{ km}^2$  box showing the location of this experiment. (b) A zoomed-in view within this box, with terrain height as background color field. The DOW radar is located at Battle Pass, in the center of the map. The white circles show the locations of the AgI generators (SM $nn$ ). Several instrument sites over and upwind of the Sierra Madre are also shown.

## 2. Experimental design and instrumentation

### a. Experimental design

The ASCII campaign was conducted over the Sierra Madre in southern Wyoming from January to March of 2012. The WWMPP operated eight AgI generators upwind of this mountain, denoted as SM $nn$  in Fig. 1. The typical low-level flow in winter storms in this area is southwesterly, snowfall occurs frequently, and supercooled liquid water is common in clouds over the mountain (Ritzman 2013; Breed et al. 2014).

A description of the ASCII experimental design and instruments on the ground and aboard the University of Wyoming King Air aircraft (UWKA) can be found in Geerts et al. (2013). The DOW was located at Battle Pass (a Continental Divide pass), with good low-elevation views toward the southwest and east. An elevated platform surrounded by trees and located  $\sim 500 \text{ m}$  downwind of the DOW (“Battle town site”) hosted a vertically pointing Micro Rain Radar (MRR), an

Environmental Technologies, Inc. (ETI) snow gauge, and several hydrometeor particle sampling instruments (Geerts et al. 2013). Geonor, Inc., and ETI snow gauges were deployed at several other sites as part of the WWMPP. During each intensive observation period (IOP), GPS Advanced Upper-Air Sounding (GAUS) rawinsondes were launched from Dixon, Wyoming, in the valley upwind of the Sierra Madre every 2 h (Fig. 1) to measure the ambient humidity, temperature, and wind profiles. A dual-frequency passive microwave radiometer, pointing at a low elevation angle from Savery, Wyoming, over the Sierra Madre, measured liquid water path (LWP).

DOW data were collected in 12 IOPs during ASCII. Three of them (18 January, 14 February, and the first one on 28 February) were excluded because of lack of echoes, a wind shift associated with a frontal passage, and/or significant changes in precipitation type. The other nine IOPs are separated into two groups on the basis of DOW radar echo structure and WCR vertical velocity transects: in three IOPs that are examined in Jing and Geerts (2015) the WCR vertical velocity transects reveal narrow convective updrafts exceeding  $1 \text{ m s}^{-1}$  (Houze 1993) over the depth of the cloud, and the DOW echoes are convective or include embedded convective cells. The definition of “convective” precipitation using a map of DOW base reflectivity is not based on an algorithm that spatially separates stratiform from convective regions, as in Cunningham and Yuter (2014) but rather is just a subjective confirmation of a classification of an entire IOP, a classification that is primarily based on WCR vertical transects.

In the six remaining IOPs, which are the subject of this paper (Part I), the WCR dual-Doppler velocity transects that are aligned with the wind (i.e., across the mountain) reveal stratified flow on the upwind side and more stratiform reflectivity patterns. In all six IOPs, once this flow approached the mountain crest it started to sink and accelerated at low levels, resulting in the clearing of the radar echoes. Geerts et al. (2015) also analyzed reflectivity and Doppler velocity fields from the WCR in 13 winter storms over an adjacent mountain in Wyoming and found stratified flow, accelerating and plunging into the lee, to be present in approximately one-half of the cases.

### b. Weather conditions

The ambient weather conditions of the six mostly stratiform IOPs are summarized in Table 1. Much of the information in this table is based on the soundings launched from Dixon. The rawinsondes drift with the wind, but they all reached the tropopause before drifting across the Sierra Madre crest. The value for Brunt–Väisälä (B–V) frequency  $N$  listed in Table 1 is a height-weighted average of  $N_{\text{dry}}$  and  $N_{\text{moist}}$ ; the dry value ( $N_{\text{dry}}$ ) applies

TABLE 1. Summary of the upstream environment for the six IOPs. Most of the information is derived from a series of radiosondes released from Dixon (Fig. 1) during the IOPs. Average values are calculated from 3–4 soundings. The Froude number  $Fr$  is calculated as the wind speed divided by the B–V frequency  $N$  and the height of Bridger Peak above Dixon. The Richardson number  $Ri$  is the square of  $N$  divided by the square of the wind shear. LWP is inferred from a passive microwave radiometer at Savery. The mean liquid-equivalent snowfall rate  $S$  during NOSEED is estimated both from the DOW mean reflectivity between 0 and 1.5 km in the target areas and from an ETI gauge at the Battle town site. The  $Z$ – $S$  relation used is  $Z = aS^b$ , with  $a = 100$  and  $b = 1.5$  (Matrosov et al. 2009). The cloud-top temperature  $CTT$  is derived from the DOW mean echo-top height in the target areas, converted to temperature using sounding data. Here, speed is wind speed and dir is wind direction.

Date	700 hPa			LCL		Avg from surface to Bridger Peak elev (3354 m)					DOW	ETI gauge	$CTT$ (°C)	
	$T$ (°C)	Speed ( $m s^{-1}$ )	Dir (°)	$T$ (°C)	Alt (m MSL)	Speed ( $m s^{-1}$ )	Dir (°)	$N$ ( $10^{-2} s^{-1}$ )	$Fr$	$Ri$	LWP (mm)	$S$ ( $mm h^{-1}$ )		$S$ ( $mm h^{-1}$ )
19 Jan 2012	−2.6	23.3	242	−4.9	3331	18.9	237	0.88	1.7	1.17	0.15	0.21	0.46	−14
11 Feb 2012	−5.5	14.0	286	−1.9	2537	12.6	268	0.86	1.2	0.98	0.07	0.36	0.42	−27
21 Feb 2012	−8.4	15.5	260	−7.4	2917	15.9	251	0.68	1.9	0.30	0.22	0.32	0.28	−13
22 Feb 2012	−4.6	23.3	273	−3.2	2870	20.5	260	0.84	2.0	0.22	0.31	0.15	0.31	−11
29 Feb 2012	−9.5	19.0	219	−9.8	3012	18.3	213	0.49	3.1	0.28	0.12	0.20	0.06	−19
3 Mar 2012	−11.4	16.0	274	−9.1	2767	14.6	266	0.94	2.1	0.35	0.08	0.54	0.58	−18

between the surface and cloud base [i.e., lifting condensation level (LCL)], and the moist value ( $N_{moist}$ ) is the value between the LCL and the height of Bridger Peak, the highest point in the Sierra Madre. The average  $N$  remains below  $10^{-2} s^{-1}$  in all IOPs.

The 700-hPa temperature varied from  $-11.6^{\circ}$  to  $-2.6^{\circ}C$  (Table 1). Note that the elevation of Battle Pass (3034 m) was within 50 m of the 700-hPa level in all IOPs. Air passing over Battle Pass thus cooled to at least this temperature before warming in the lee. Parcels of air lifted to the top of the PBL cooled by an additional  $\sim 5$  K, since the PBL was  $\sim 600$  m deep, on average, according to WCR vertical velocity data (Geerts et al. 2013). In most of the cases, the resulting temperature is deemed cold enough for ground-based AgI seeding to be effective (Breed et al. 2014). An exception was 19 January, on which day the temperature of  $-2.6^{\circ}C$  at 700 hPa may have been too warm for effective cloud seeding. Strong winds prevailed during all IOPs, ranging from 13 to  $21 m s^{-1}$  between the surface and mountain-top level. This, along with the low stability, results in a bulk Froude number that exceeds unity in all cases (Table 1). Thus the upwind low-level air is expected to be advected across the mountain. Liquid water was present in all cases in clouds over the Sierra Madre, according to flight-level and microwave radiometer data. The radiometer-estimated LWP generally was at most 0.3 mm (Table 1), which is low relative to many storms that were seeded as part of the WWMPP (Breed et al. 2014). The mean snowfall rate  $S$  ( $mm h^{-1}$ ) in Table 1 over the mountain was low, with  $\leq 0.6 mm h^{-1}$  water equivalent in all IOPs, according to both point gauge and area-averaged DOW reflectivity estimates. The cloud-top temperature in Table 1 is derived from the DOW mean echo-top height, converted to temperature using sounding data. Most storms

were relatively shallow (topping out at 3–4 km above the terrain), with a cloud-top temperature warmer than  $-20^{\circ}C$  in all but one case (11 February). Clouds with tops colder than  $-25^{\circ}C$  are deemed unsuitable for glaciogenic seeding because of natural seeding from aloft (Grant and Elliott 1974; Manton and Warren 2011). In general, considerable variation in all parameters was observed. This may allow some insight into the conditions that are most suitable for glaciogenic seeding, although this insight will at best be speculative, given the small sample size (six cases).

c. DOW radar

The DOW radar deployed in ASCII (DOW7) is a dual-polarization X-band (3 cm) Doppler radar mounted on a truck, with a  $0.93^{\circ}$ -beamwidth volume-scanning antenna. The radar operated with 800 range gates with a fixed pulse length of 60 m, resulting in a maximum range of 48 km. The radar performed a 10-min cycle, consisting of a full-volume scan starting at  $-1^{\circ}$  elevation, followed by several vertical transects [range–height indicator (RHI)] along the direction of the low-level wind, and a vertical profile. Each cycle contains 41 elevation angles (every  $1^{\circ}$  from  $-1^{\circ}$  to  $20^{\circ}$ , every  $2^{\circ}$  from  $20^{\circ}$  to  $30^{\circ}$ , every  $4^{\circ}$  from  $30^{\circ}$  to  $70^{\circ}$ , and four  $85^{\circ}$  scans) and six  $180^{\circ}$  RHI scans (one along the wind, and two  $\pm 10^{\circ}$  off the wind direction in the up- and downwind direction).

The DOW was located at Battle Pass, shown as a black star in Fig. 1. This is an excellent site for low-elevation radar coverage both downwind and upwind of the AgI generators and beyond. The  $-1^{\circ}$  elevation angle is unblocked in a narrow window to the west-southwest and in a broader one to the east and northeast (Fig. 2). Battle Pass is surrounded by slightly higher terrain to the northwest and the southeast. This terrain is cleared by DOW elevation angles above  $3^{\circ}$  to the northwest and  $6^{\circ}$

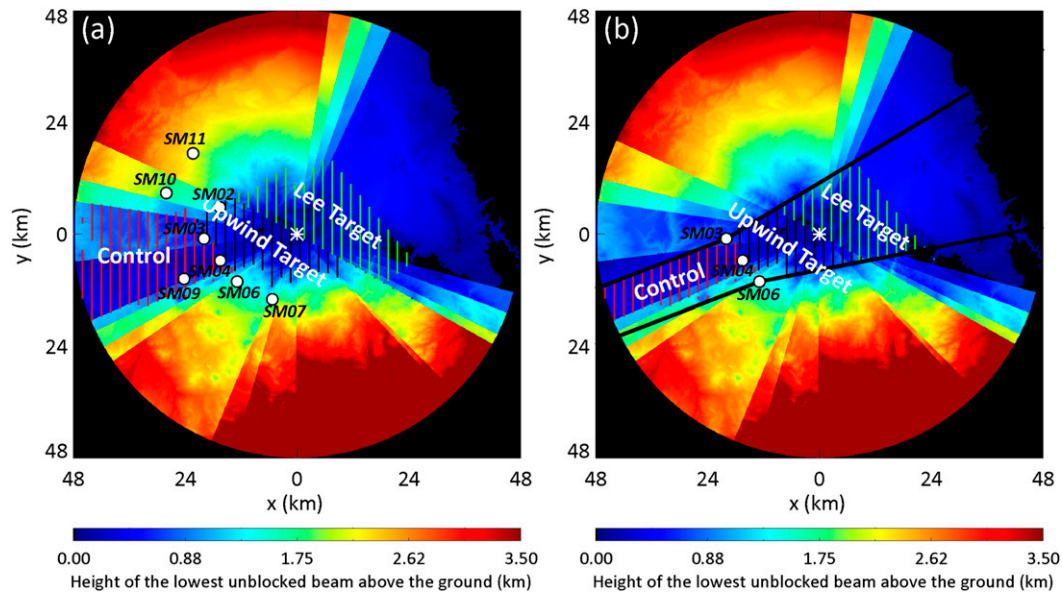


FIG. 2. Height (km AGL) of the lowest unblocked DOW beam. The vertical hatchings show the location of the control (red), upwind target (black), and lee target (green) areas in the case of (a) seven or eight AgI generators (white circles) and (b) just three generators. The boundaries are fixed for eight-generator IOPs [the situation in (a)] but pivot with the mean wind direction when only three generators were activated [the situation in (b)]. The black lines upstream of the generators in (b) show the IOP-specific mean wind direction, and those downstream of the generators are rotated out by  $10^\circ$ .

to the southeast. At the low-elevation scans, the return power at many radar gates is suspect because of ground clutter, contamination from radar side lobes, anomalous propagation of the radar beam, and other interferences with the terrain. We removed ground clutter using a fuzzy-logic algorithm that is based on the density function for snow and ground clutter (Gourley et al. 2007; J. Aikins 2014, personal communication).

To examine the radar variables at different height levels, the DOW spherical-coordinate data (range, azimuth, and elevation) were interpolated onto a Cartesian grid using the National Center for Atmospheric Research's "Reorder" software (Oye et al. 1995). We chose resolutions of 1000, 1000, and 100 m in the zonal, meridional, and vertical directions, respectively, using a Cressman weighting scheme with radii of influence of 1000, 1000, and 200 m within 20-km range and 1000, 1000, and 400 m outside this range. The vertical radii of influence are the smallest values that avoid gaps in the grid from beam spreading. A high vertical resolution is desired to allow examination of vertical profiles of reflectivity and other variables. Fine horizontal resolution is not needed in this study.

### 3. Analysis method

To assess possible seeding impact, two regions are defined (Fig. 2): 1) *control* (unaffected by seeding) and 2) *target* (affected by seeding). The control area is

upwind of the AgI generators and thus is in the foothills of the Sierra Madre. No suitable lateral control area, over the mountain but to the side of the AgI nuclei plumes, was available, given the lack of low-elevation DOW data near the Sierra Madre crest north and south of Battle Pass (Fig. 2b). The target region is further partitioned into two parts, one upwind of the Sierra Madre crest (denoted as *upwind target*) and one in the lee (denoted as *lee target*), to allow examination of the dependence of seeding impact on fetch and also to quantify seeding impact in terms of watersheds, because the Sierra Madre is a Continental Divide range. The average distance between the three core AgI generators and the Sierra Madre crest near Battle Pass is 18 km. (This is the approximate width of the upwind target area.) The boundaries of the three regions are determined in part by the height of the lowest unblocked DOW beam above the ground (Fig. 2).

Some IOPs employed all available<sup>1</sup> AgI generators, whereas others used just three core generators (SM03, SM04, and SM06) (Table 2; Fig. 1). For the "all generator" IOPs, the control region is defined as a region

<sup>1</sup> Three IOPs (11 February, 21 February, and 3 March) intended to deploy all eight generators, but in two of them SM11 did not fire and therefore only seven generators were used, as shown in Table 2.

TABLE 2. Summary of seeding impact analysis method for the six cases. Shown are the start and end times (UTC) of the DOW volume scans included in the NOSEED and SEED periods and the duration of each period (h; in parentheses), the time delay (min) used from the time the generators were activated, the number of generators used, and the sequence of NOSEED and SEED periods. The time delays for AgI activation are estimated from the average wind speed shown in Table 1. The number of AgI generators activated was three (SM03, SM04, and SM06), seven (all generators except SM11) or eight (all generators).

Date	NOSEED	SEED	Time delay for control area	Time delay for upwind target area	Time delay for lee target area	No. of AgI generators	Sequence
19 Jan 2012	1433–1812 (3.7)	1812–2021 (2.1)	0	10	20	3	NOSEED then SEED
11 Feb 2012	0136–0447 (3.2)	0447–0807 (3.3)	0	20	30	8	NOSEED then SEED
21 Feb 2012	1917–2117 (2.0)	2117–2339 (2.3)	0	20	30	7	NOSEED then SEED
22 Feb 2012	1308–1511 (2.1)	1511–1732 (2.3)	0	10	20	3	NOSEED then SEED
29 Feb 2012	0121–0322 (2.0)	2150–2359 (2.1)	0	10	20	3	SEED then NOSEED
3 Mar 2012	1731–1925 (2.0)	1925–2157 (2.5)	0	20	30	7	NOSEED then SEED

upwind of most AgI generators in which the lowest unblocked DOW beam is no more than 1 km above ground level (AGL; Fig. 2a). This threshold of 1 km AGL was chosen because the well-mixed PBL was found to be at most  $\sim 1.0$  km deep (Geerts et al. 2013). The eastern boundary of the control region is 1 km downstream of generators SM03, SM04, and SM06 (Fig. 1). Although a very small part of the control area is thus located downstream of the generators, it is unlikely that the AgI plumes from these generators can reach the DOW volume, because they are  $\sim 600$  m below the lowest DOW beam. The upwind target region is downwind of the generators yet upwind of the mountain crest, and the lee target region is downstream of the crest (Fig. 2). The same threshold of 1 km AGL for the lowest unblocked DOW beam is used to delineate the other boundaries of the two treated regions.

For IOPs with just three AgI generators (SM03, SM04, and SM06) in operation (Fig. 2b), the study areas are narrowed on the basis of the expected dispersal of AgI nuclei. Observational studies (Holroyd et al. 1988; Huggins 2007) and modeling work (Chu et al. 2014) suggest that AgI seeding plumes tend to be narrow. In this paper, we choose to use a dispersion angle of  $\pm 10^\circ$ . Areas outside this dispersion angle are assumed to be unaffected by AgI seeding. The along-wind boundaries for the control area are lines parallel to the mean wind direction on the upstream side of the AgI generators, ending at SM03 and SM06, as shown in Fig. 2b. On the downwind side of the generators, the along-wind boundaries for the target areas are designed as the mean wind direction  $\pm 10^\circ$ . The crosswind boundaries of the control region, upwind target region, and lee target region are the same as for the all-generator IOPs. These regions are slightly different in the various IOPs because of differing mean wind directions (Table 1).

In each IOP an untreated period (NOSEED) is compared with a treated (SEED) period. The NOSEED and

SEED time periods for different IOPs are shown in Table 2. Some time is needed for AgI dispersion and activation, and therefore a delay is applied in the target regions that is based on the mean wind speed. This delay is an integral multiple of 10 min, the DOW scan-cycle period. The NOSEED period precedes the SEED periods in all but one case. On 29 February, the SEED period precedes the NOSEED period. This requires a buffer period ( $\sim 1.5$  h) because of the lingering presence of AgI nuclei (e.g., Holroyd et al. 1988).

The seeding impact is assessed as the temporal change (SEED – NOSEED) of reflectivity and differential reflectivity observed by the DOW in the target region in comparison with the same temporal change in the control region. The basic assumption for this double-difference method is that the natural trend in cloud and precipitation properties is the same in the control and target areas. We will assess the validity of this assumption for all six IOPs. This assumption requires steady upstream conditions and steady flow over the mountain. Forecast storm steadiness was a key criterion in the IOP calling procedure. Even so, natural variability of precipitation will be the main source of uncertainty in this study. Another assumption is that the sampling periods shown in Table 2 are long enough to allow assembly of a representative distribution of precipitation echoes in the three regions; that is, the period needs to be long enough to encompass small-scale variations within the storm but short enough not to include periods outside the storm duration. The AgI generators were activated for  $\sim 2$  h for the three-generator IOPs and for  $\sim 4$  h for the all-generator IOPs (Table 2). The DOW did not operate during the entire 4-h seeding periods. In effect the SEED period for DOW data analysis was 2.1–3.3 h long, and the NOSEED period was then chosen to be of nearly equal length. The steadiness and representativeness assumptions are more likely to be satisfied in stratiform

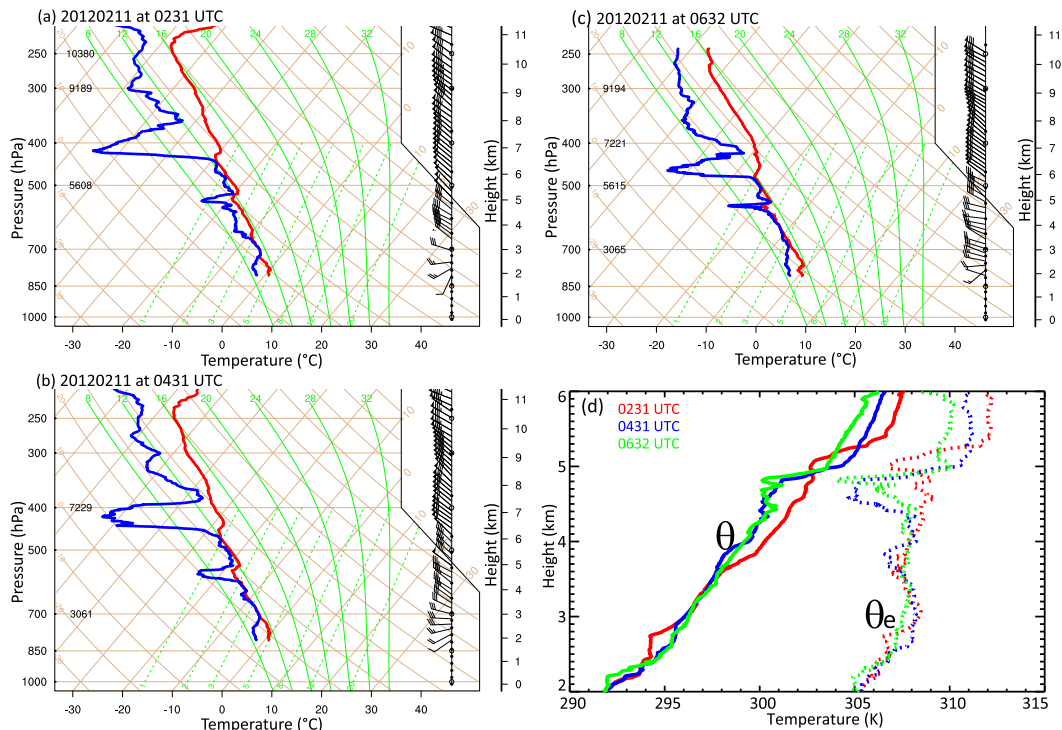


FIG. 3. Skew  $T$ -log $p$  diagrams of data from rawinsondes released from Dixon on 11 Feb 2012 (a),(b) in the NOSEED period and (c) in the SEED period. The red (blue) lines show the temperature (dewpoint) profiles. The wind profile is shown to the right; a full barb represents  $5 \text{ m s}^{-1}$  ( $\sim 10 \text{ kt}$ ). (d) Vertical profiles of potential temperature  $\theta$  and equivalent potential temperature  $\theta_e$  for the three soundings.

precipitation, which is spatially more uniform and is often more persistent.

#### 4. A case study—11 February 2012

The orographic cloud on 11 February 2012 (IOP7; Geerts et al. 2013) was dominated by stratiform precipitation with embedded stronger echoes. No WCR data are available for this case.

##### a. Ambient weather conditions and storm characteristics

Three rawinsondes were launched from Dixon during IOP7 (Figs. 3a–c). The vertical profiles of potential temperature  $\theta$  and equivalent potential temperature  $\theta_e$  are shown in Fig. 3d. Here  $\theta_e$  is computed on the basis of Eq. (2.34) in Markowski and Richardson (2010). The three soundings are averaged to obtain the parameters in Table 1.

The surface and low-level wind was weaker during IOP7 than during any other IOP in this study, but it was still strong enough to yield a bulk Froude number of 1.2 (Table 1). The 10-m wind speed at Dixon was  $4\text{--}5 \text{ m s}^{-1}$  from the southwest during the IOP, according to

weather-station data. The wind veered from the surface to mountaintop level ( $\sim 665 \text{ hPa}$ ), where the wind direction was northwesterly. The wind profile was steady across the three soundings.

The soundings suggest a possible decoupling of a 200–300-m-deep surface layer from the flow aloft, possibly because of nighttime surface cooling or because of snow sublimation. A nearly saturated, moist-neutral layer between  $\sim 720 \text{ hPa}$  (2.8 km MSL) and  $\sim 530 \text{ hPa}$  (5.0 km MSL) signifies the orographic cloud. This layer is evident as having a nearly constant  $\theta_e$  (Fig. 3d). A large portion of this layer is saturated with respect to water and supersaturated with respect to ice, including the dendritic-growth zone (approximately  $-15^\circ\text{C}$ ), at least in two of the three soundings.

The timeline of ambient and cloud-precipitation structure parameters for this IOP is shown in Fig. 4. The direction of the mean low-level wind measured by sounding ranged between  $260^\circ$  and  $280^\circ$ , close to the surface wind direction at Battle Pass. The average surface wind speed at Battle Pass was  $\sim 12 \text{ m s}^{-1}$ , much stronger than in the upwind valley ( $4.5 \text{ m s}^{-1}$ ). The effective B–V frequency, Froude number, precipitable water, and LCL height were all steady, suggesting

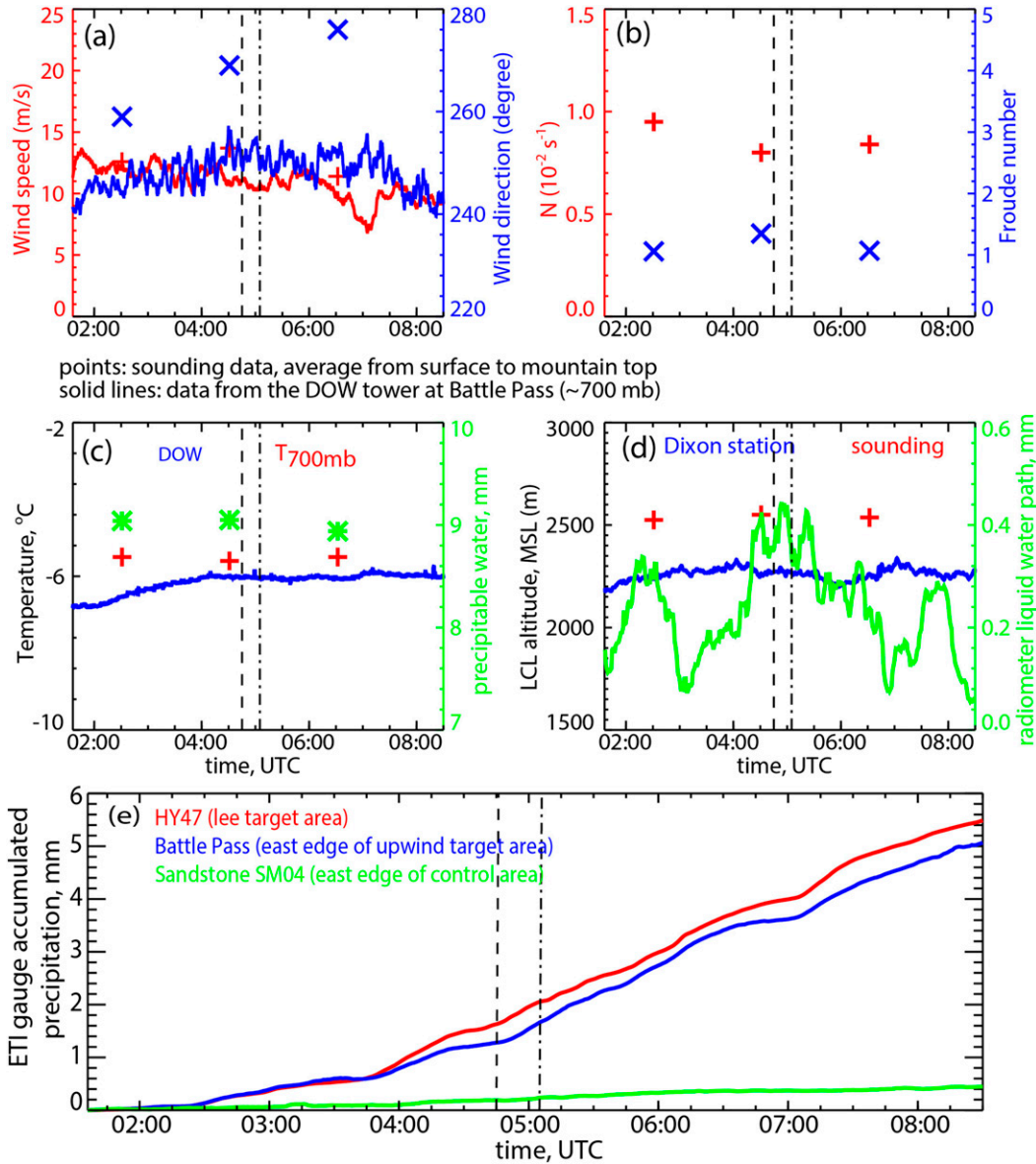


FIG. 4. Evolution of several atmospheric parameters during the course of IOP7 on 11 Feb 2012, as measured by rawinsondes, a passive microwave radiometer, weather stations, and snow gauges at locations in the upwind foothills and on the mountain. The vertical dashed line shows the activation time of the AgI generators, and the dashed-dotted line shows the estimated arrival time of the AgI plume at Battle Pass. The three gauge locations are shown in Fig. 1.

persistence of basic flow and precipitation characteristics (Fig. 4). The B–V frequency computed between 300 m AGL (not ground level) and mountaintop level is only approximately  $0.3 \times 10^{-2} \text{ s}^{-1}$ , suggesting little flow stratification above the shallow stable layer. The temperature at Battle Pass was steady at approximately  $-6^\circ\text{C}$ . The average radiometer LWP was very low (0.2 mm), even though the cloud was deeper on this day than for any other of the six IOPs. Between the first and the third sounding (a period of 2 h), the

cloud-base height increased and the cloud-top height decreased, according to the soundings (Fig. 3). The echo-top height also decreased, as will be shown later. Yet the precipitation rate increased (Fig. 4e). The changes are benign. Here we are examining natural trends, but the increase in snowfall rate during SEED at Battle Pass and at HY47, downwind of the AgI generators, may be due to seeding, of course.

Snow photography at the Battle town site shows many dendrites, sometimes rimed, and some cone-shaped

graupel particles, mainly during NOSEED (prior to 0447 UTC). Early in the IOP the precipitation was mostly shallow, with almost no precipitation at Battle Pass before 0210 UTC. Between 0220 and 0340 UTC deep cloud and heavy precipitation occurred, the MRR at the Battle town site revealed echoes at as high as  $\sim 2250$  m AGL, and some cells had reflectivity values of  $\sim 30$  dBZ (not shown).

Basic storm characteristics of IOP7 are illustrated with a DOW  $0^\circ$ -elevation-angle base reflectivity map, as well as along-wind RHI scans of  $Z$ , ZDR, and radial velocity (Fig. 5). The domain of the reflectivity map in Fig. 5a exactly matches that of the terrain map in Fig. 1, and therefore terrain influences can be examined. The sampling area at  $0^\circ$  elevation angle is relatively small, but it is obvious that the precipitation is generally stratiform over the Sierra Madre. The stronger echoes ( $Z > 20$  dBZ) at the east end of the DOW scanning domain (Figs. 5a,b) are upwind of the Medicine Bow range (Fig. 1), which is not part of this study. The echoes upwind of Battle Pass (toward the west) are not uniform. Vertical cross sections of radar reflectivity indicate narrow vertically aligned reflectivity stacks (Fig. 5b). Their vertical velocity properties are unknown because the UWKA did not fly on this day. These cells become better defined and more intense in the following 2 h (not shown).

The DOW echo top reached as high as 3.5 km above DOW level (6.5 km MSL). Low-level echoes were confined to the mountain. The echo-free wedge in the lee of the Sierra Madre (Fig. 5b) suggests subsidence in the lowest 2 km above DOW level. The difference between outbound and inbound radial velocities (Fig. 5d) indicates that this subsiding flow accelerated across the crest. Later DOW RHI scans (not shown) show decreasing cloud depth but fairly steady low-level echoes throughout the IOP, which is consistent with the sounding data. ZDR values are very small, indicating that ice particles are randomly oriented.

### b. Exploring a seeding signature

To examine changes in vertical structure, frequency-by-altitude diagrams (FADs; Yuter and Houze 1995) of equivalent reflectivity  $Z$  are plotted for two periods and three regions (Fig. 6). Height is expressed above local ground level. The ground level is considered as the reference level because the PBL depth and isentropes generally follow the terrain. Since the control region is at a lower altitude than the DOW and the lowest elevation angle of the DOW is  $-1^\circ$ , no data are available below  $\sim 500$  m AGL in the control region (Fig. 2). The vertical resolution in all of the FADs is 100 m. The horizontal resolution is 0.5 dBZ. The count in any bin

is normalized by the total count at that particular level AGL. This method, unlike the 2D normalization used in other studies (e.g., Geerts et al. 2010), keeps the  $Z$  distribution at a certain level unaffected by that at other levels, and therefore precipitation changes near the surface can be examined without any influence from echo changes aloft. The drawback of this 1D-normalization method is that it emphasizes the frequencies at levels at which few echoes exist, for example, near cloud top. Therefore awareness of the data presence at each level is important. This presence is expressed as a fraction ranging between 0% and 100% (the yellow line in Fig. 6). The mean  $Z$  profiles in Fig. 6 are computed in units of  $Z$  ( $\text{mm}^6 \text{m}^{-3}$ ) and not dBZ. Echo-free areas (which were common, especially in the control area; see Figs. 5a and 6a) are not counted in the average.

The mean low-level  $Z$  is much higher in the upwind target area than in the control area, consistent with the difference in surface precipitation rate in these areas (Fig. 4e). The reflectivity increases toward the ground in the target regions, indicating low-level growth, but it does not in the control region, in either period (Fig. 6). In the lee, the mean  $Z$  is suppressed between 0.5 and 2.0 km AGL (Fig. 6g) relative to the upwind side (Fig. 6d) as a result of subsidence. These are basic precipitation growth and decay signals across a mountain. We are interested in the temporal difference of reflectivity frequency (SEED – NOSEED) in each region. During SEED, the mean low-level  $Z$  increased by 2 dB in the upwind target area (Fig. 6f), which is well above the DOW's reflectivity uncertainty due to temporal drift ( $\sim 0.1$  dB from start to end of IOP). The difference FAD in the upwind target area (Fig. 6f) shows more obvious dipoles below  $\sim 2$  km: the blue (red) region on the right (left) in Fig. 6f suggests a higher low-level  $Z$  on average during SEED. Some low-level precipitation enhancement is evident also at greater fetch from the generators (Fig. 6i), but the magnitude in the lee target region is smaller than that in the upwind target region. No low-level enhancement occurred in the control region (Fig. 6c).

To examine the spatial distribution of the low-level precipitation change, the mean  $Z$  between 0 and 1.5 km AGL is examined for NOSEED and SEED separately (Fig. 7). First it is pointed out that during the entire IOP the sample size (i.e., number of pixels with  $Z > 0$  dBZ) in the control region is much smaller than that in the target regions (Figs. 7d,e), on account of the greater radar range and lower terrain elevation. Thus the averages shown in Figs. 7a–c are less robust in the control region. As expected of a stratiform orographic cloud,  $Z$  increases as air rises toward the mountain crest and then rapidly

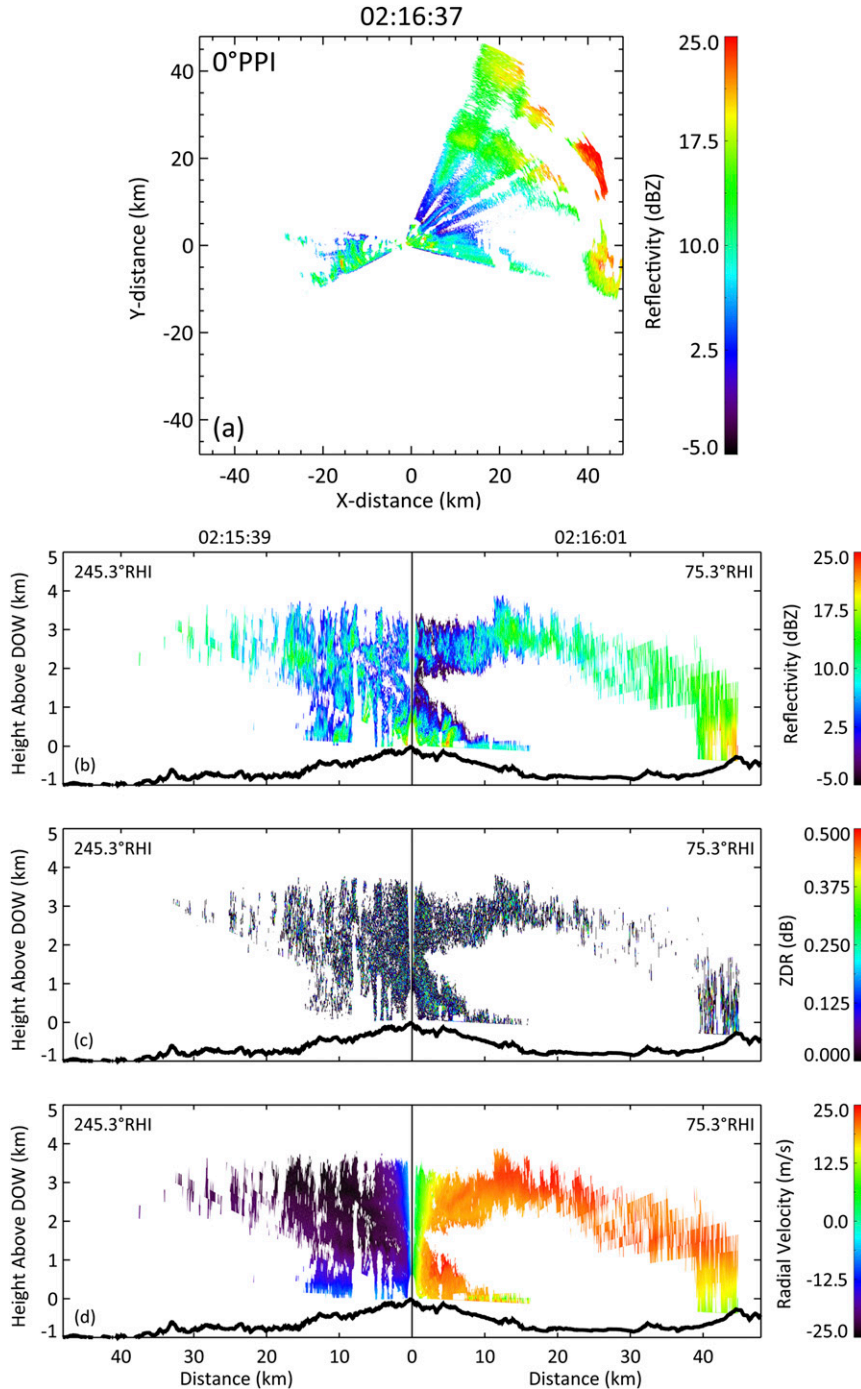


FIG. 5. Example of DOW data, collected at ~0216 UTC 11 Feb 2012, during the NOSEED period: (a) 0° base reflectivity map; RHI scan of (b) reflectivity, (c) differential reflectivity, and (d) radial velocity. The RHI scan is from WSW (left) to ENE (right), approximately aligned with the low-level wind. The exact azimuth angles are shown. They are not exactly 180° apart but rather are in the direction of best -0.5°-elevation coverage. The underlying terrain profile is added in the RHI scans.

decreases as air sinks in the lee (Figs. 7a,b). The low-level Z apparently increases downwind of the AgI generators during SEED, mainly some 10–15 km from the generators, according to the difference map (Fig. 7c). In short,

the low-level Z increases by 1–2 dB on average in the upwind target region (Figs. 6f and 7c). This may be a seeding signature. We cannot prove the attribution since the natural trend during SEED can be different in the

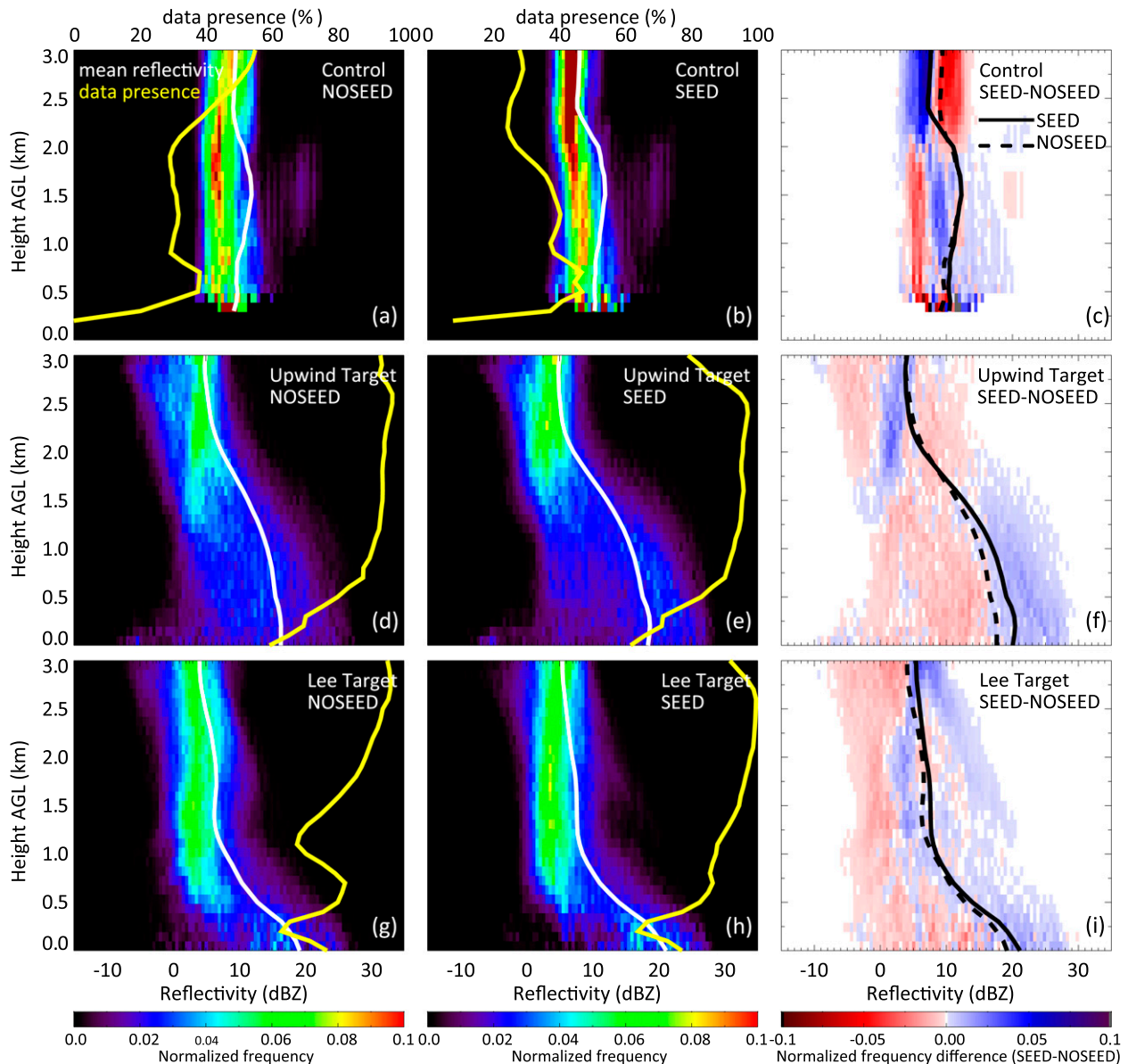


FIG. 6. Normalized FADs of DOW reflectivity above local ground level for the 11 Feb 2012 case study for (left) the NOSEED period, (center) the SEED period, and (right) the difference (SEED – NOSEED) in the (a)–(c) control, (d)–(f) upwind target, and (g)–(i) lee target regions. The average reflectivity profiles are shown as white lines and the data presence of NOSEED and SEED periods for the three areas is shown as yellow lines in (a),(b),(d),(e),(g), and (h). The average reflectivity profiles are shown as black lines in (c),(f), and (i).

control and the target areas, but the magnitude of this change is consistent with numerical simulations of the seeding impact in a case over the Medicine Bow range (Chu et al. 2014).

### c. Exploring growth mechanisms for snow

The dynamic-seeding mechanism (see section 1) has been examined mainly for convective clouds. This AgI-mediated hydrometeor-growth mechanism is unlikely

to be active in stratiform clouds because of lack of buoyancy even when AgI nuclei cause glaciation. For instance, low-level snowfall rate was enhanced during seeding in the 21 February 2012 IOP, a stratified flow case, even though the cloud-top height decreased (Pokharel et al. 2014a).

Similar results are found in IOP7 (Fig. 8), although the cloud layer was close to moist neutral and some isolated small convective cells may have been present.

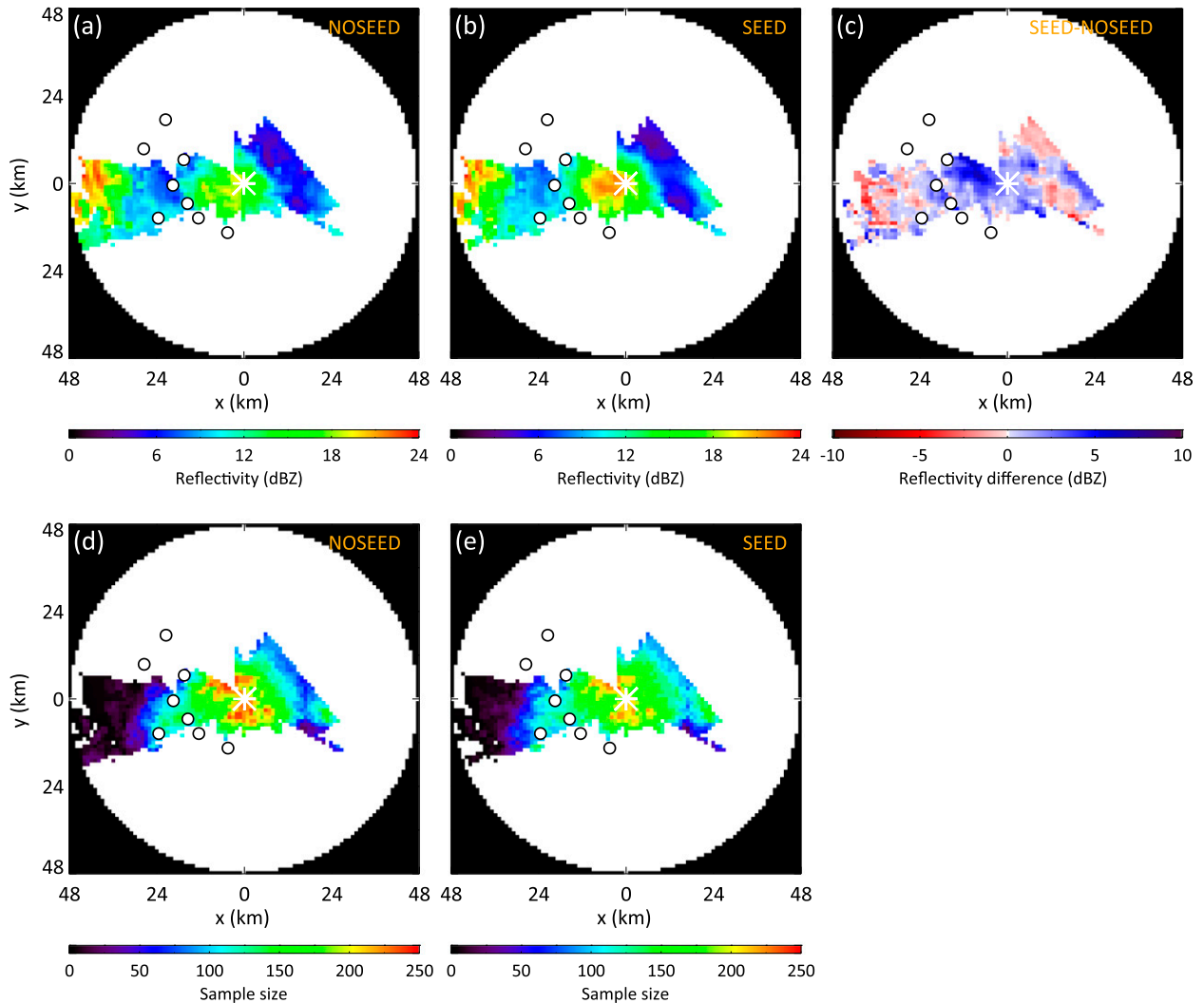


FIG. 7. Mean low-level reflectivity maps for the 11 Feb 2012 case study: (a) the NOSEED period, (b) the SEED period, and (c) the change (SEED – NOSEED). All reflectivity values between 0.0 and 1.5 km AGL are averaged. Also shown are the sample sizes for the (d) NOSEED and (e) SEED periods. The asterisk indicates the location of DOW, and the circles locate the AgI generators.

Figures 8a–c show the DOW echo-top height AGL, and Figs. 8d–f show the echo-top height in MSL and corresponding cloud-top temperatures as based on the nearest sounding data (Fig. 3). Echo tops rise as the flow approaches the mountain. A deep lee wave is present east of the crest. The echo top decreased everywhere over time (Fig. 8f), which is consistent with the upwind sounding data. The most significant cloud-top decrease is found in the control region, and the least significant cloud-top decrease is found in the upwind target region. (The density of echo-top data is just as high in the control region as in the target regions, and therefore this comparison is more robust than the low-level reflectivity change discussed in section 4b.) We see these changes as natural trends. It is extremely unlikely that the

suppressed echo-top subsidence in the target region is due to ground-based seeding.

There are some changes in snow properties at low levels that may be attributable to seeding. Plummer et al. (2010) and Que et al. (2013) show that in mixed-phase clouds ZDR tends to be larger if snow is generated mainly through vapor diffusion (the Bergeron process) whereas ZDR tends to be smaller if riming dominates. Also, dry aggregates tend to have a near-zero ZDR and larger Z, whereas dendrites and plates tend to have a positive ZDR (since they tend to fall horizontally) and a lower Z (Vivekanandan et al. 1994; Thompson et al. 2014). Thus ZDR may reveal changes in snow-growth mechanisms. The injection of ice nuclei in cloud encourages growth by vapor diffusion, because

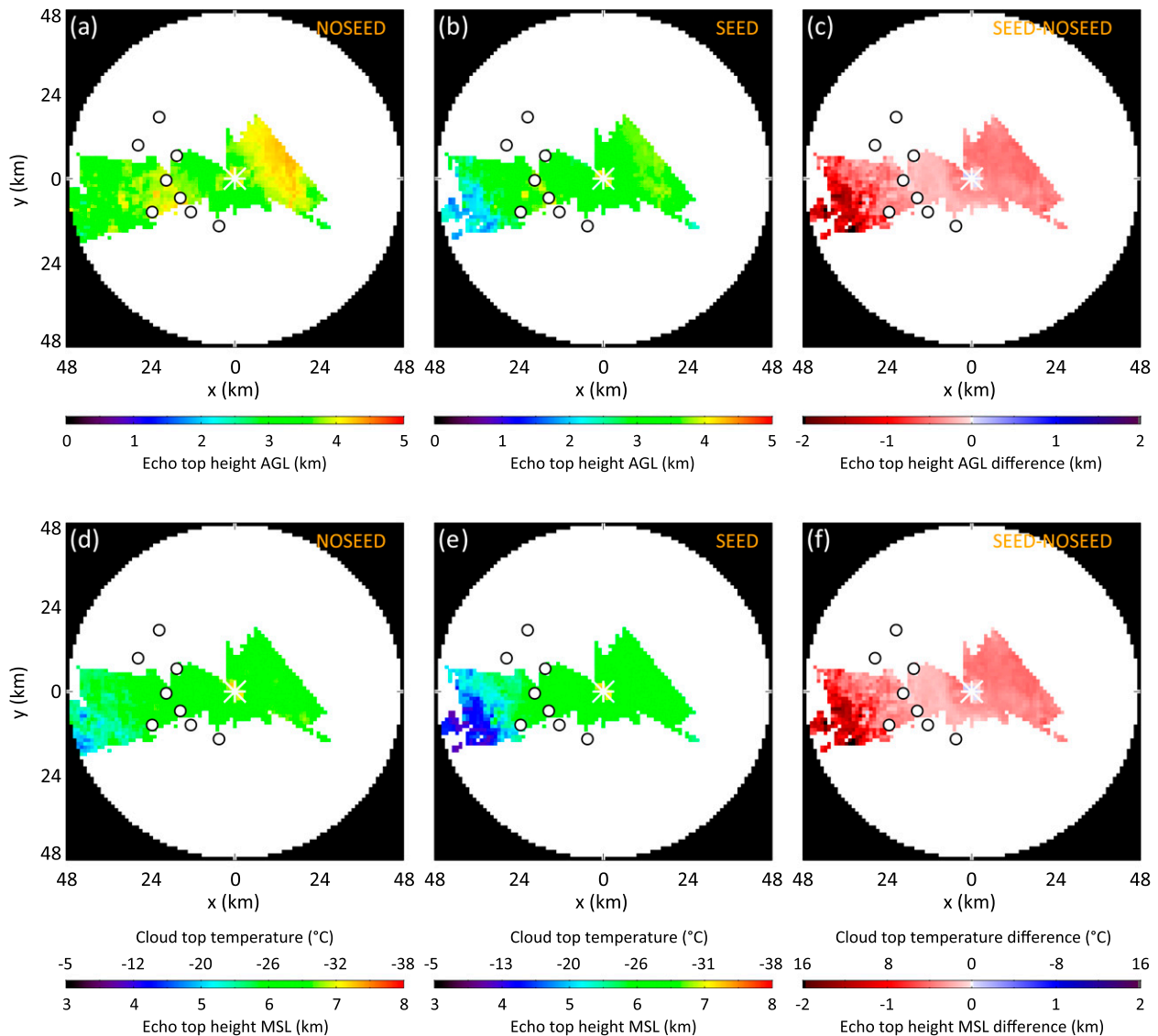


FIG. 8. The average DOW echo-top height AGL of (a) the NOSEED period, (b) the SEED period, and (c) the change (SEED – NOSEED) for the 11 Feb IOP. (d)–(f) Similar to (a)–(c), but for the echo-top height MSL, with an indicative cloud-top temperature added to the color-key bars below. The asterisk indicates the location of DOW, and the circles are the AgI generators.

of a reduced mean distance between ice crystals, and a reduced chance for droplets to grow to a size sufficient for growth by riming. Therefore less riming on snow particles and more vapor diffusion are expected during SEED. ZDR may be increased also by the more numerous ice crystals during SEED, growing as dendrites or plates. The correlation coefficient between copolar returns  $\rho_{HV}$  quantifies the complex correlation (phase and power) of the received horizontal and vertical signals from the transmitted pulses: for a pulse volume in which all particles are perfect spheres,  $\rho_{HV}$  is equal to 1, whereas for a pulse volume that is dominated by irregular particles such as ice crystals with variable shapes,

$\rho_{HV}$  can be as low as 0.8 (e.g., Vivekanandan et al. 1999). For low values of  $Z$  ( $< \sim 10$  dBZ), both ZDR and  $\rho_{HV}$  generally increase with  $Z$ . In a Rayleigh-scattering regime, polarization variables such as ZDR and  $\rho_{HV}$  are biased toward the largest particles in a resolution volume.

Figure 9 shows typical along-wind RHI scans of  $Z$ , ZDR, and  $\rho_{HV}$  measured during NOSEED and SEED. During NOSEED,  $Z$  and ZDR are small and the low-level  $\rho_{HV}$  is large. During SEED, however,  $Z$  and ZDR values are larger and  $\rho_{HV}$  is smaller at low levels over the mountain. These changes suggest larger, more horizontally oriented snowflakes and fewer rimed particles

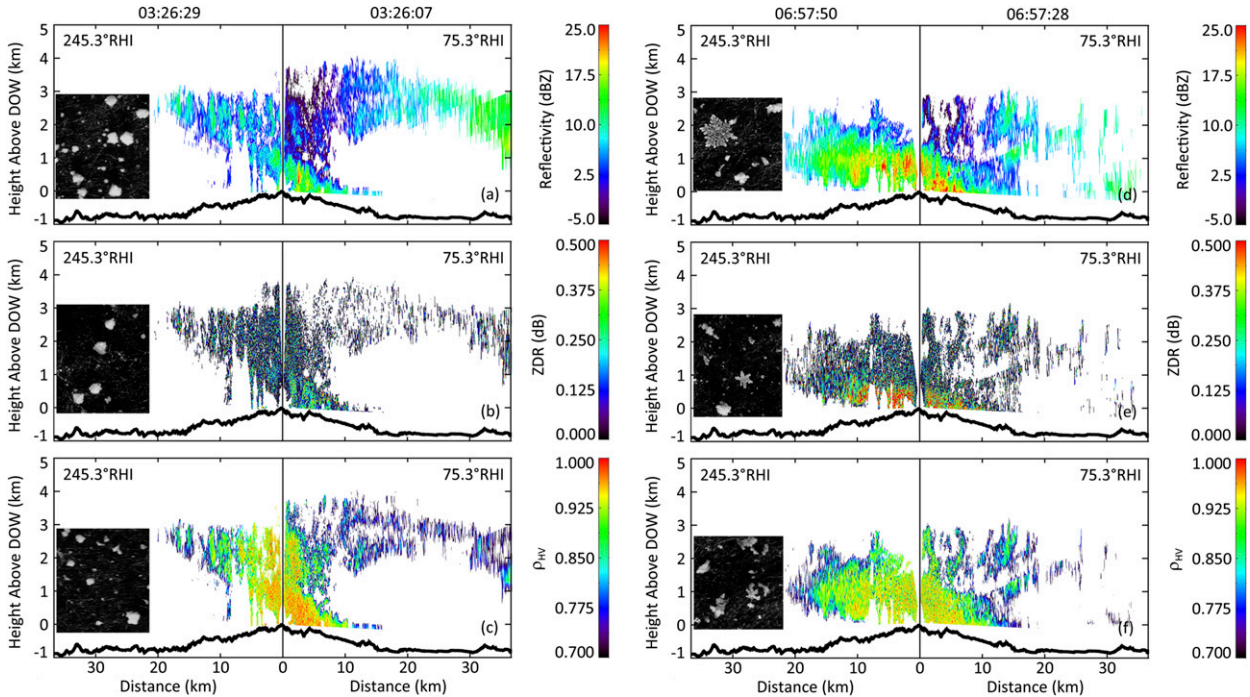


FIG. 9. Typical RHI scan examples of (a),(d) DOW reflectivity, (b),(e) differential reflectivity ZDR, and (c),(f) correlation coefficient  $\rho_{HV}$  for the 11 Feb IOP in the (left) NOSEED and (right) SEED periods. The RHIs are roughly along the low-level wind, from WSW (left) to ENE (right). Six photographs taken manually at the Battle town site at nearly the same times show typical snow shapes.

during SEED. The large ( $\sim 0.5$  dB) ZDR values just above the mountain may indicate predominantly dendrites and plates. The decrease in  $\rho_{HV}$  at low levels is interpreted as a transition from more spherical, rimed particles during NOSEED to unrimed crystals during SEED. Some examples of snow-crystal photography at the Battle town site are embedded in Figs. 9a–f. They confirm the presence of rimed particles during NOSEED and mainly unrimed snowflakes and some fairly large dendritic ice crystals during SEED, which confirms that the Bergeron growth process is more significant during SEED.

The composite ZDR FADs for IOP7 are displayed in Fig. 10. ZDR analysis is only useful for low, quasi-horizontal elevation angles, and therefore data from high-elevation scans ( $>10^\circ$ ) are excluded from the interpolation to a Cartesian grid. The vertical resolution of these FADs is 100 m, the horizontal resolution is 0.05 dB, and the data are normalized by the number of pixel at each level, as was done for the Z FADs (Fig. 6). Low-level ZDR values increase from the foothills (control) to the mountain (target), both during NOSEED and SEED, consistent with the increase in Z. The ZDR-difference FADs show no obvious change in the control region, but in the upwind target region ZDR increased by  $\sim 0.1$  dB at low levels, which indicates

more dendrites or plates. This mean change is within the uncertainty of the ZDR measurement of the DOW. It is a relative difference over time and not an absolute value of ZDR. Polarization measurements of a calibration target may drift over time, but zenith ZDR measurements, conducted every 10 min, do not show a significant drift during this IOP.

To examine the relationship between Z and ZDR at low levels (0–1.5 km AGL), the reflectivity frequency distribution is plotted as function of ZDR (Fig. 11). Here frequencies are normalized per Z bin; that is, the sum of all pixel values for a given value of Z is equal to 1. The purpose is to examine changes in ZDR in isolation from changes in Z (or precipitation rate), since Z and ZDR are correlated. ZDR is fairly narrowly distributed for given Z values. ZDR remains mostly constant for larger Z values and decreases with increasing Z beyond  $\sim 20$  dBZ. The latter may be due to increased riming fractions in the convection-generating cells. The Z–ZDR relation hardly changes from NOSEED to SEED in the control region (Fig. 11c). ZDR increases in most of the Z bins (5–30 dBZ) in the upwind target area during SEED (Fig. 11f). This result indicates more depositional growth of ice crystals, especially dendrites and plates, for a given value of Z. ZDR decreases in most of the Z bins in the lee target area during SEED

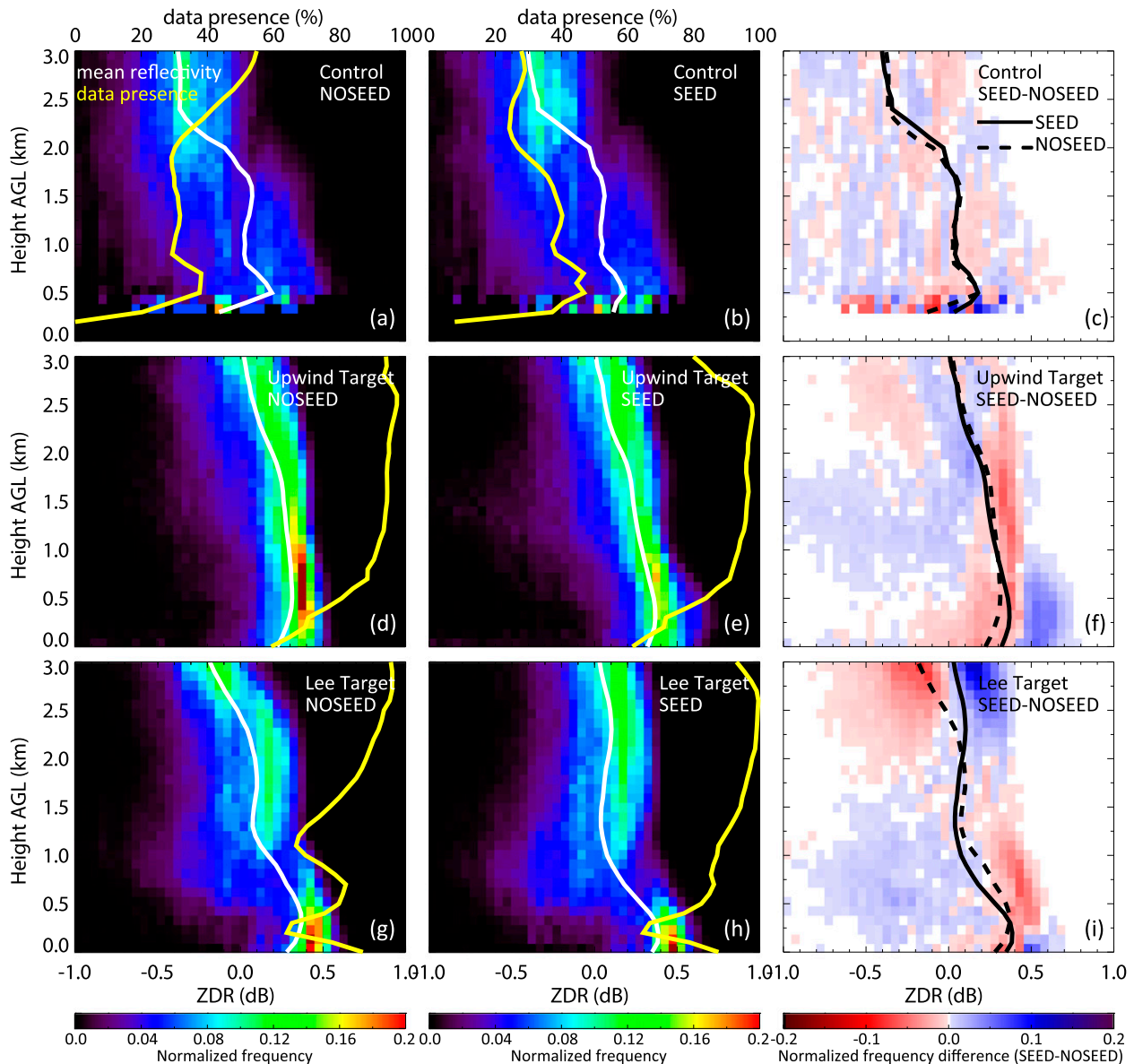


FIG. 10. As in Fig. 6, but for ZDR.

(Fig. 11i). This behavior is consistent with that seen in the ZDR FADs, in which the ZDR only increases below  $\sim 300$  m AGL and decreases between 0.3 and 1.5 km (Fig. 10i) whereas Z increases at all levels below 1.5 km AGL (Fig. 6i).

In short, evidence from FADs of Z (Fig. 6) and ZDR (Fig. 10), mapped low-level Z (Fig. 7), displays of ZDR versus Z (Fig. 11), and snow photography at the Battle town site (Fig. 9) suggests a possible seeding signature in the upwind target region, with significant Z and ZDR increases at low levels, a ZDR increase for most Z values, and mostly unrimed large dendritic ice crystals and aggregates on the ground. These changes happened

during seeding, notwithstanding a decrease in cloud-top height across the region (Fig. 8). Any seeding signature is weaker and shallower in the lee target region. It is clear that the observed changes cannot unequivocally be attributed to seeding. They do warrant more dual-polarization radar measurements of glaciogenically seeded clouds.

## 5. Composite analysis

### a. Evolution of orographic precipitation

As mentioned before, the key assumption in the attribution of a seeding impact on precipitation is that the

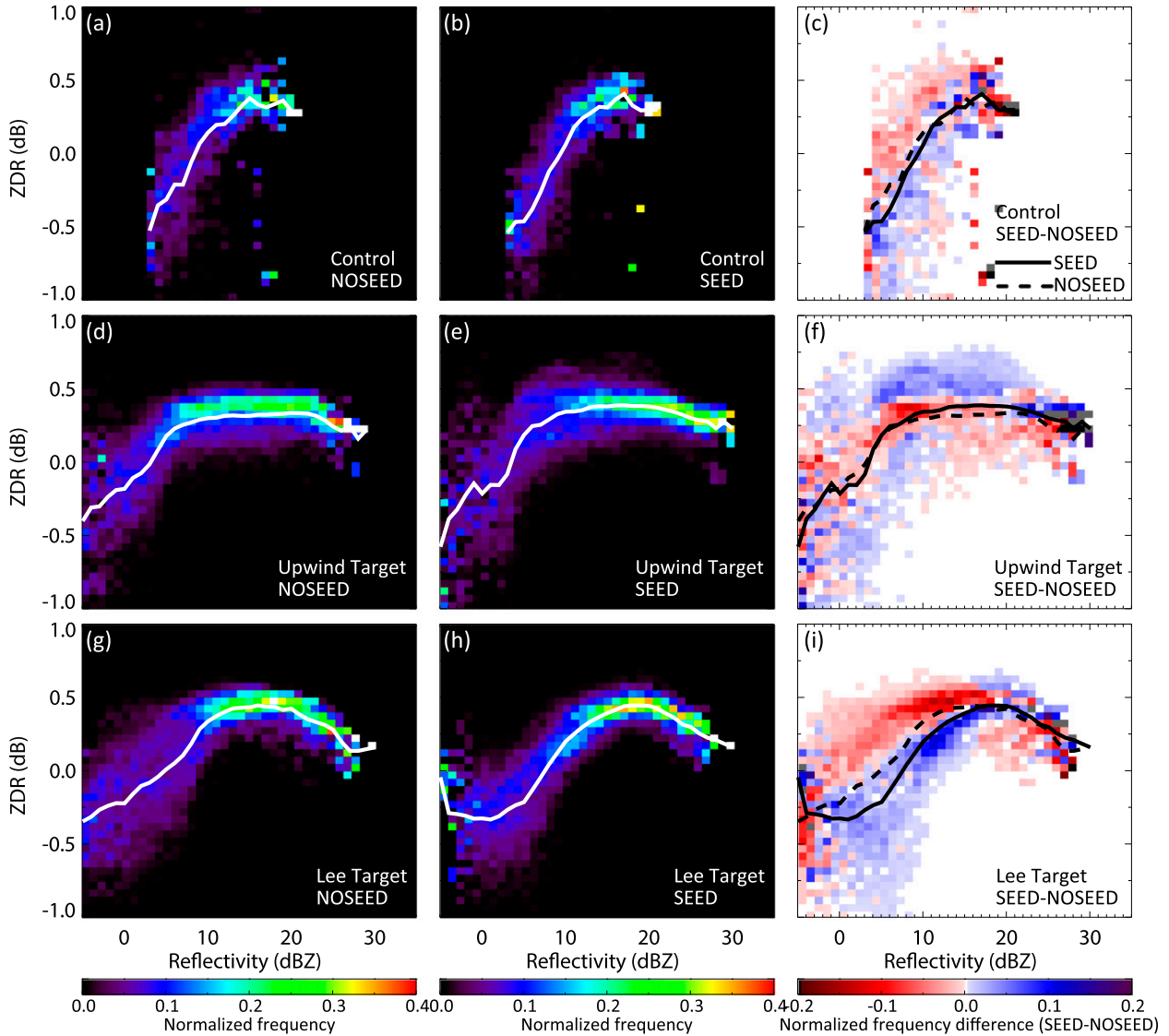


FIG. 11. Normalized frequency of reflectivity  $Z$  by  $ZDR$  for the control, upwind target, and lee target regions, during the (a),(d),(g) NOSEED and (b),(e),(h) SEED periods in IOP7. The bin resolution of  $Z$  ( $ZDR$ ) is 1 dB (0.05 dB). (c),(f),(i) The frequency difference (SEED – NOSEED). Only points within 1.5 km AGL are included in the count. The white lines in (a),(b),(d),(e),(g) and (h) [repeated as black lines in (c),(f), and (i)] represent the average  $ZDR$  for any  $Z$  value.

natural trends are the same in the control and target areas. Figure 12 provides an overview of the precipitation evolution in the control and target areas during NOSEED and SEED periods. The snowfall rate  $S$  ( $\text{mm h}^{-1}$ ) is derived from the DOW reflectivity  $Z$  ( $\text{mm}^6 \text{m}^{-3}$ ) averaged between 0.5 and 1.5 km AGL, using the relation  $S = 0.046Z^{0.67}$  (Matrosov et al. 2009). We choose 0.5–1.5 km AGL because the DOW hardly “sees” below 0.5 km AGL in the control area (Fig. 2) and because reflectivity in the layer from 0.5 to 1.5 km AGL still represents precipitation characteristics in the boundary layer. The snowfall rate is computed locally and then averaged over the area of

interest; reflectivity values below approximately  $-5$  dBZ imply a zero precipitation rate. The precipitation series in the control and target areas show similar natural trends (Fig. 12), suggesting similar local precipitation evolution. The correlation is better even when one allows a 10–20-min lag for the target region, to account for advection of precipitation echoes. A seeding signature is not obvious from Fig. 12, which is not surprising since it is small relative to the natural variations. The evolution of orographic precipitation differs among different IOPs (Fig. 12). On 19 January and 22 February, the precipitation is about the same in the control and target areas, but in the former IOP

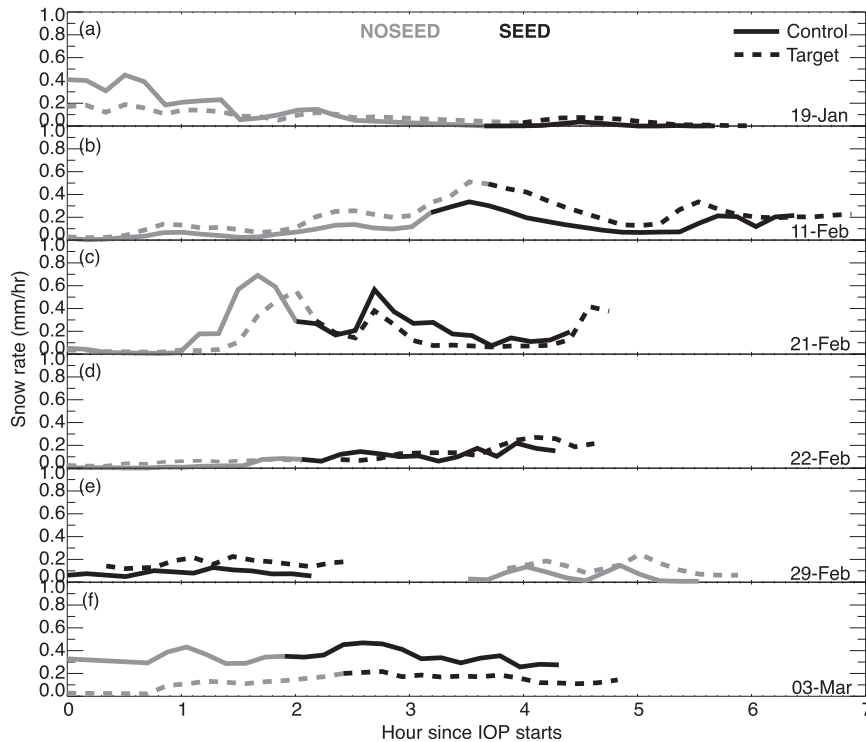


FIG. 12. Time series of the average snowfall rate derived from 0.5 to 1.5 km AGL reflectivity in the control and target areas for the six IOPs.

the storm weakens and in the latter it intensifies during SEED. On 21 February and 3 March, the precipitation intensity in the target area is smaller than that in the (foothills) control area, suggesting a stronger upwind influence of the mountain. On 11 and 29 February, the precipitation intensified as clouds moved from the foothills to the target areas—that is, positive orographic enhancement. In short, different storms evolve differently during NOSEED and SEED periods and from foothills to higher-elevation terrain. In all six IOPs, however, the trends are similar in the control and target regions. Also, the spatial autocorrelation is very high across the two regions: it is larger than 0.6 on average within both regions for the reference point SM04 (Fig. 1) for all six IOPs. In two IOPs (19 January and 21 February) the autocorrelation is larger than 0.9. In short, the basic assumption that the natural trends in control and target areas are similar is valid, but they are not quite the same.

#### b. Changes in low-level reflectivity

Normalized FADs of reflectivity or any other variable can readily be composited for multiple IOPs. The ambient and cloud conditions of six stratiform storms were described in section 2b. Analyses of the type shown in Fig. 4 were done for each storm to ascertain that conditions remained steady during the IOP. The composite

Z FADs for these six IOPs are displayed in Fig. 13, using analysis methods that were identical to those in Fig. 6. The spread is broader than in a single IOP FAD since storms with different intensities are combined. The data presence (yellow line in Figs. 13a and 13b) is very low in the control region, indicating patchy echoes. On average, higher Z is found on the upwind side of the mountain (Figs. 13a,d), suggesting that most precipitation in stratiform storms falls upwind of the crest and that low-level growth is stronger in the upwind target area than in the control area. Reflectivity at ~1 km AGL decreases rapidly with distance between the upwind and lee target areas (Figs. 13d,g), indicative of snow sublimation in subsiding air. Again, these are expected signatures of orographic snow growth and decay.

For SEED – NOSEED changes, the Z-difference FADs show opposite dipoles between the control and target regions at low levels. During SEED, Z (and thus precipitation rate) decreased on average in the control region while it increased in the target regions. Also, similar to the FADs for IOP7 (Fig. 6), the low-level Z enhancement during SEED is larger at close range from the generators (upwind target) (Fig. 13f) than at greater fetch (lee target) (Fig. 13i). Because mixing in stratiform clouds is limited to the turbulent boundary layer (Geerts

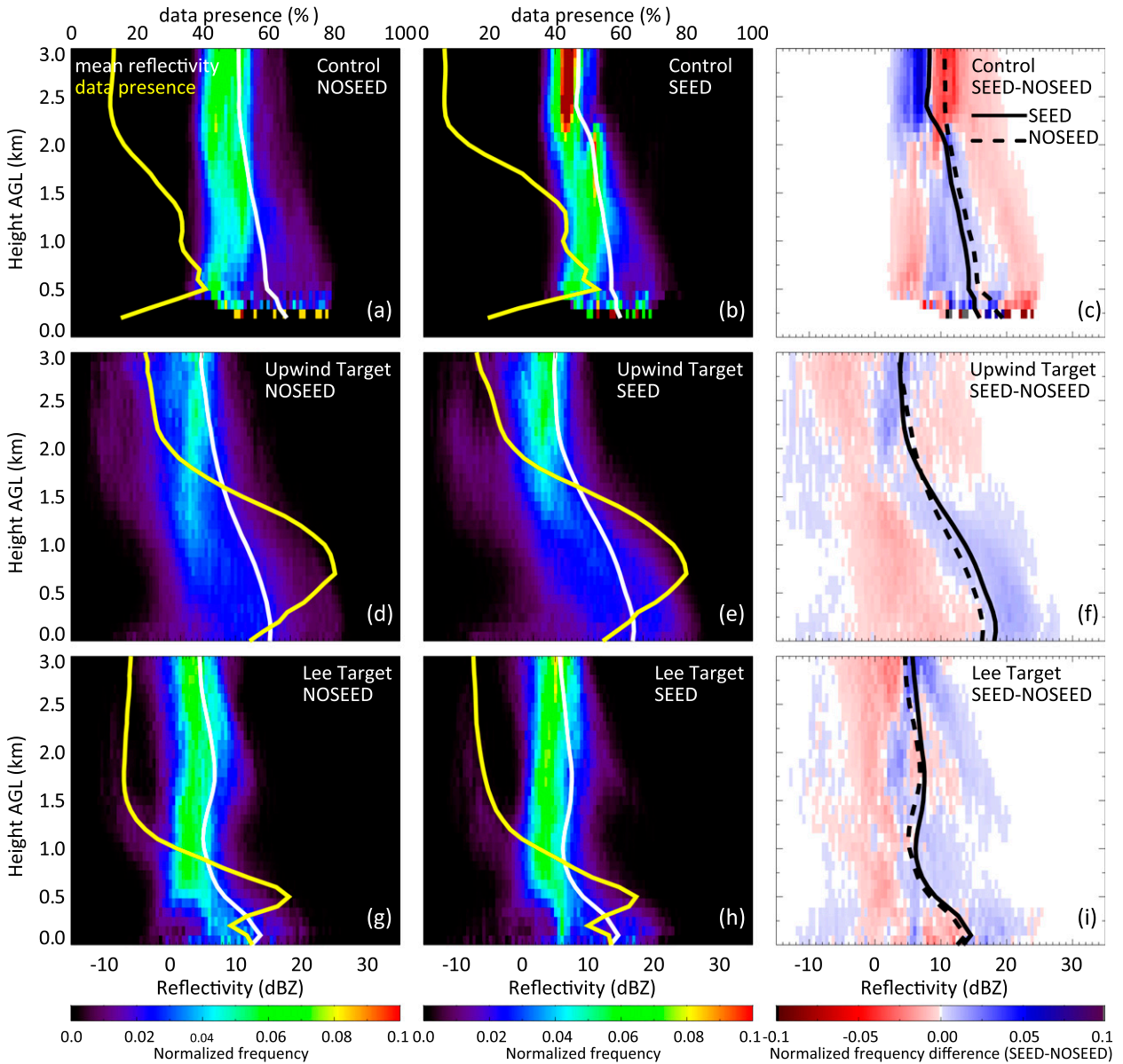


FIG. 13. As in Fig. 6, but for all six cases combined.

et al. 2011), which in the ASCII IOPs was ~0.6 km deep (Geerts et al. 2013), changes above ~1 km AGL clearly cannot be attributed to ground-based seeding; rather, they indicate natural trends between two periods.

The average Z maps for 0–1.5 km AGL for the six stratiform cases are shown in Fig. 14. A layer depth of 1.5 km is chosen because there are very few echoes below 1.0 km AGL in the control area. Thus a deeper, but still shallow, layer is more suitable to describe the natural trend in the control area. A shallower region can be used for the target areas, but the results are essentially the same as in Fig. 14. The Z (and thus total precipitation) are

mostly uniform on the upwind side while they rapidly weaken on the lee side, consistent with the stratiform cases examined over the adjacent Medicine Bow range by Geerts et al. (2015). At the surface the leeward drying may be a little slower than is suggested by Fig. 14a since very shallow Z maxima are often observed in the lee (Fig. 13g). This spillover is due to an accelerating, subsiding current that is commonly observed in strong-wind stratified-flow cases (Geerts et al. 2015).

The observed low-level temporal change (SEED – NOSEED) in Z in the upwind target region in comparison with the change in the control region (Fig. 13)

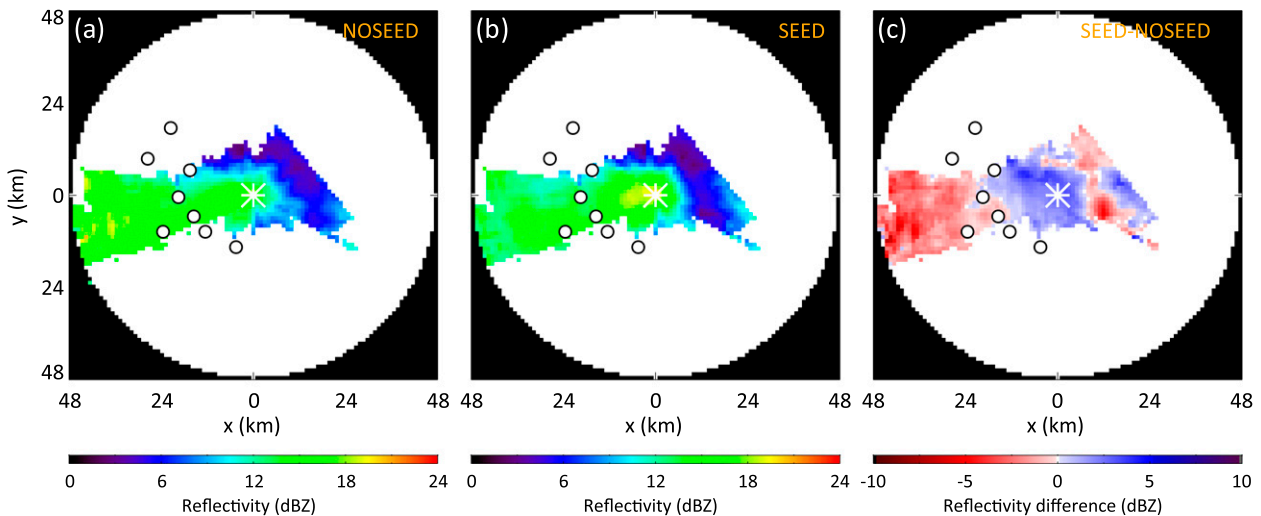


FIG. 14. As in Figs. 7a–c, but for all six cases.

suggests that seeding may increase  $Z$  and thus snowfall rate. Although low-level  $Z$  generally decreases between the two periods, it increases starting a few kilometers downwind of the core AgI generators (Fig. 14). This increase extends mainly over the mountain, where the DOW data density is best. The positive change tapers off quickly in the lee, suggesting that the optimal seeding fetch is short and is comparable to the distance to the crest ( $\sim 18$  km). The optimal seeding fetch probably depends on wind speed and on the geometry of the target mountain, and on the related extent of supercooled liquid water clouds. Certainly these low-level changes may at least partly reflect natural trends in the precipitation field. The attribution to AgI seeding is not definitive, given the natural variability of precipitation and the small dataset. We now examine echo-top-height evolution and dual-polarization variables, seeking further evidence for attribution.

### c. Changes in ZDR

We now examine changes in the six-IOP composite ZDR profiles. The average low-level ZDR values have little change in the control region while slightly increasing in the target regions (Fig. 15), roughly consistent with IOP7 (Fig. 10). Such an increase suggests relatively more horizontally oriented snowflakes, and more snow growth through the Bergeron process. Any changes in low-level ZDR distribution in the primary target region (Fig. 15b) are small, however; in other words, seeding does not seem to impart a significant change on the shape and orientation of snowflakes. Not all six cases show an increase of ZDR during seeding in the upwind target region. In particular, it decreased on 22 February, a shallow case with large LWC and strong

wind and therefore intense PBL turbulence (Table 1). In this case, low-level ZDR values were lower (near zero) during SEED because of the larger LWP and existence of large droplets (larger than  $25 \mu\text{m}$  in size). Riming may remain the dominant low-level snow-growth mechanism in this case, even during SEED. More stratiform cases are needed to better understand the impact of seeding on dual-polarization variables in orographic echoes.

To investigate any systematic changes in ZDR for a given  $Z$ , the low-level (0–1.5 km AGL) ZDR is plotted as a function of  $Z$  for all six cases (Fig. 16), using the same compositing technique as for IOP7 (Fig. 11). The spread in ZDR differences is larger for the composite analysis relative to IOP7, suggesting a broader diversity in crystal shapes and riming fractions in the various storms. ZDR tends to increase with  $Z$  even for larger values of  $Z$ , as compared with IOP7. In focusing on the SEED – NOSEED difference, it is seen that ZDR is  $\sim 0.2$  dB larger for given  $Z$  values (where reflectivity  $> 10$  dBZ) in the target areas (Figs. 16b,c). This is not observed in the control area and is consistent with Fig. 13f and Fig. 14c. This result suggests that ZDR increases because of a higher concentration of horizontally oriented ice crystals, such as dendrites and plates, and fewer rimed particles during AgI seeding.

In short, ZDR varies considerably from storm to storm and within storms, but composite changes between NOSEED and SEED periods are small. These small changes suggest that seeding tends to enhance  $Z$  and snow growth by vapor diffusion in stratiform orographic clouds, mostly at short fetch from the ground-based generators, but this weak seeding signature could be entirely natural since the dual-polarization signal is small relative to the natural change of the cloud microphysics.

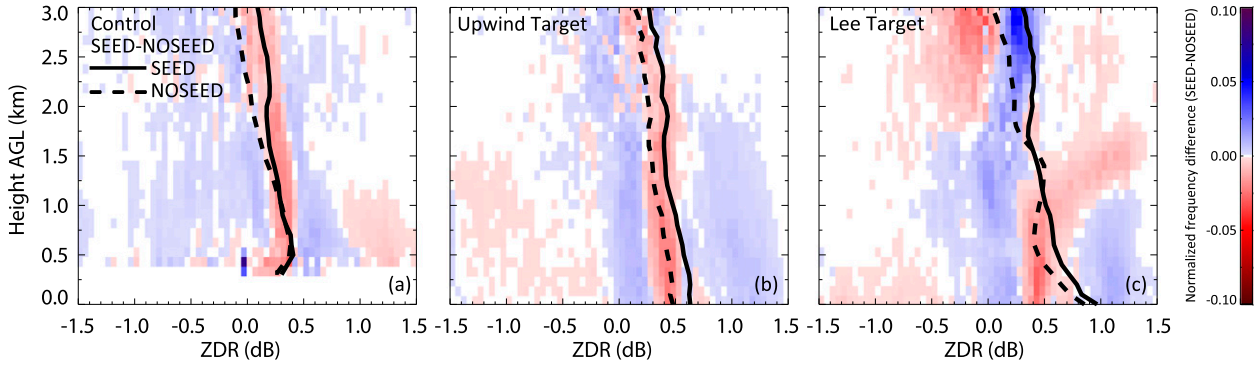


FIG. 15. Composite ZDR difference FADs of (a) the control area, (b) the upwind target area, and (c) the lee target area, for all six cases. The average ZDR profiles are shown as dashed (NOSEED) and solid (SEED) lines.

d. Seeding-impact analysis

The change of  $Z$  from NOSEED to SEED can be in part due to natural changes, related to changes in upwind conditions or simply to patchy precipitation advected through the area. If we assume that the natural evolution is the same in the control region and the target region (this assumption is examined in section 5f), then the seeding effect can be isolated. We define the reflectivity impact parameter ZIP as the difference between the downstream (target) average  $Z$  change (SEED - NOSEED) and the upstream (control)  $Z$  change (Pokharel et al. 2014a):

$$ZIP = \Delta dBZ_T - \Delta dBZ_C, \quad (1)$$

where each of the two  $\Delta dBZ$  terms comprises  $dBZ_S - dBZ_N$  (with subscripts  $S$  and  $N$  referring to SEED and NOSEED, respectively) for the indicated region and the subscripts  $T$  and  $C$  refer to the target and control regions, respectively. Here the target region can be the upwind part, the lee part, or both combined. Such double differences have been used by others to tease out a seeding effect (e.g., Gabriel 1999).

Figure 17 shows the ZIP profiles of the upwind and lee target areas (Fig. 2). The average ZIP near the surface was  $\sim 2.8$  dB ( $\sim 2.4$  dB) in the upwind target (lee target) region, corresponding to a relative precipitation increase of 54% (45%), assuming the  $Z-S$  relation that is mentioned in Table 1. All six cases show positive low-level ZIP values in the upwind target region, with a small range of ZIP values. Modeling work using the WRF Model in large-eddy-simulation mode with the Thompson microphysics scheme and an AgI seeding module (Xue et al. 2013a) for another ASCII case (Chu et al. 2014), as well as more idealized sensitivity experiments (Xue et al. 2013b), shows that the expected ZIP value is 1–2 dB for the ASCII AgI generator configuration and typical weather/cloud conditions during ASCII. Therefore, the observed ZIP values near the surface are slightly larger than the model predicted ones, but these values obviously are very sensitive to the definition of the target region.

These positive ZIP values are not confined to the PBL. In fact they extend to near cloud top, again suggesting that natural changes in cloud-top height may in part be responsible for the positive ZIP values near the surface.

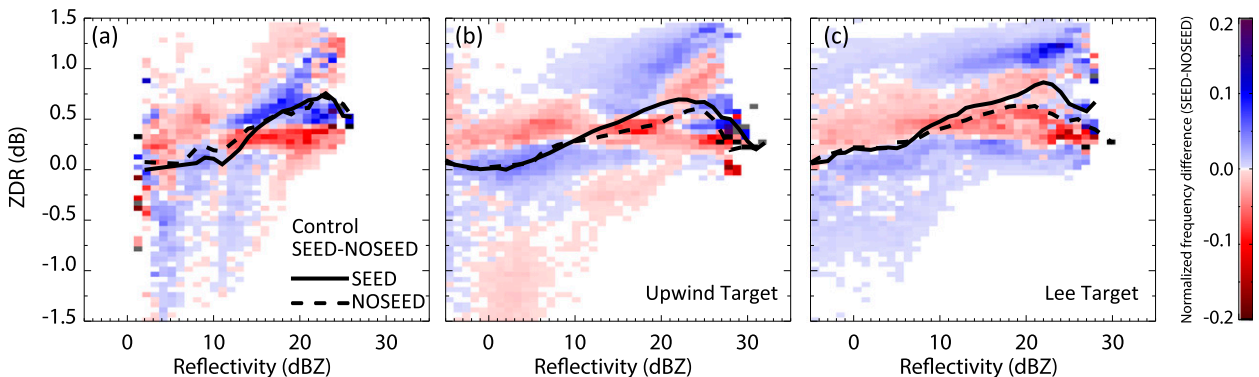


FIG. 16. As in Figs. 11c, 11f, and 11i, but for all six cases.

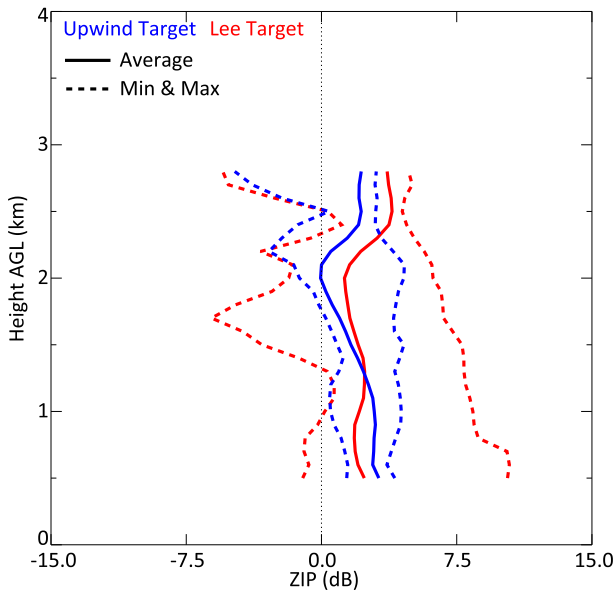


FIG. 17. The profile of ZIP, which is defined as the reflectivity change (SEED – NOSEED) in the target region relative to that in the control region. The blue lines represent the ZIP of the upwind target region, and the red lines represent the ZIP of the lee target region. The average (solid lines) refers to the six-case composite. The lowest and highest values for any of the six cases are shown as well.

#### e. Ambient and cloud conditions

Several factors can influence the efficacy of ground-based glaciogenic seeding of orographic clouds. Temperature is important because the activation of AgI and natural ice nuclei and the rate of diffusional snow growth are all temperature dependent (DeMott 1997; Breed et al. 2014). The AgI activation increases by 2.5 orders of magnitude between  $-6^{\circ}$  and  $-10^{\circ}\text{C}$  (DeMott 1997). Observational evidence suggests a relatively large ratio of liquid water content over ice water content (LWC/IWC) between  $-10^{\circ}$  and  $-5^{\circ}\text{C}$  in natural clouds but a much smaller LWC/IWC ratio between  $-15^{\circ}$  and  $-10^{\circ}\text{C}$  (Boudala et al. 2004). Both the AgI activation capacity and the LWC/IWC ratio are important to the efficiency of cloud seeding. Therefore, and because snow growth by the Bergeron process is most rapid around  $-12^{\circ}\text{C}$ , a cloud-base temperature of approximately  $-10^{\circ}\text{C}$  is expected to be suitable for precipitation increase due to AgI seeding. Liquid water content is another key parameter. In general, a higher LWC enhances precipitation more, but the suitable ranges of LWC and the related microphysical processes are poorly understood (e.g., Morrison et al. 2013). Low-level stability and wind speed can affect seeding efficiency by controlling the depth in which AgI nuclei can be mixed in the clouds. A potentially unstable atmosphere favors convection, either

isolated or embedded in stratiform precipitation. Convection yields a greater mixing depth for AgI nuclei, as well as a higher LWC and more snow-growth possibilities. The natural concentration of ice nuclei or injected ice crystals can affect AgI seeding efficiency as well. If natural ice nuclei are abundantly present in the clouds, the additional AgI nuclei will have little effect. Natural seeding mechanisms, such as the seeder–feeder mechanism (e.g., Rutledge and Hobbs 1983) or the supply of ice crystals from the ground up (Geerts et al. 2011) can thus significantly affect natural snow growth, and suppress seeding efficacy. The seeder–feeder mechanism is common in deep stratiform clouds and becomes very likely when the cloud-top temperature falls below  $-25^{\circ}\text{C}$  (Grant and Elliott 1974; Manton and Warren 2011).

With these expectations in mind, we now examine the relation between ZIP and some of these ambient and cloud conditions, with the caveat that this analysis is based on a statistically insignificant number of cases (six) that cover a narrow parameter space. Figure 18 presents ZIP as function of LWP, mean reflectivity during NOSEED in the target areas ( $\text{dBZ}_{\text{target\_noseed}}$ ),  $N$ , mean wind speed, cloud-top temperature, and cloud-base temperature. Most of these variables are listed in Table 1. ZIP is averaged from the surface to 1.5 km AGL, over the full target region. The two target areas are combined here because we explore conditions that are suitable for precipitation enhancement across the mountain range and ignore details of geographic distribution. The six-case sample suggests that ZIP increases with LWP (Fig. 18a) and also with cloud-base temperature (Fig. 18f). The temperature dependence probably is partly due to the correlation of temperature with LWP (Table 1); that is, the parameters are not examined in isolation.

ZIP appears to increase also with wind speed (Fig. 18d), again possibly because wind speed correlates positively with LWP (Table 1). Seeding may become less efficient with increasing snowfall rate ( $\text{dBZ}_{\text{target\_noseed}}$ ; Fig. 18b), maybe because of an abundance of natural ice crystals. A decrease in stability tends to increase seeding efficacy (Fig. 18c), with one outlier on 22 February. That case was relatively stable but shows a large ZIP value, possibly because of the very high LWC and a cloud top that is too warm for significant natural ice initiation (Table 1). Also, ZIP tends to increase with cloud-top temperature, as expected (Fig. 18e).

#### f. Natural trends across the target mountain range

The attribution of the double-difference parameter ZIP to AgI seeding rests on the basic assumption that the natural trend of storm structure is the same for

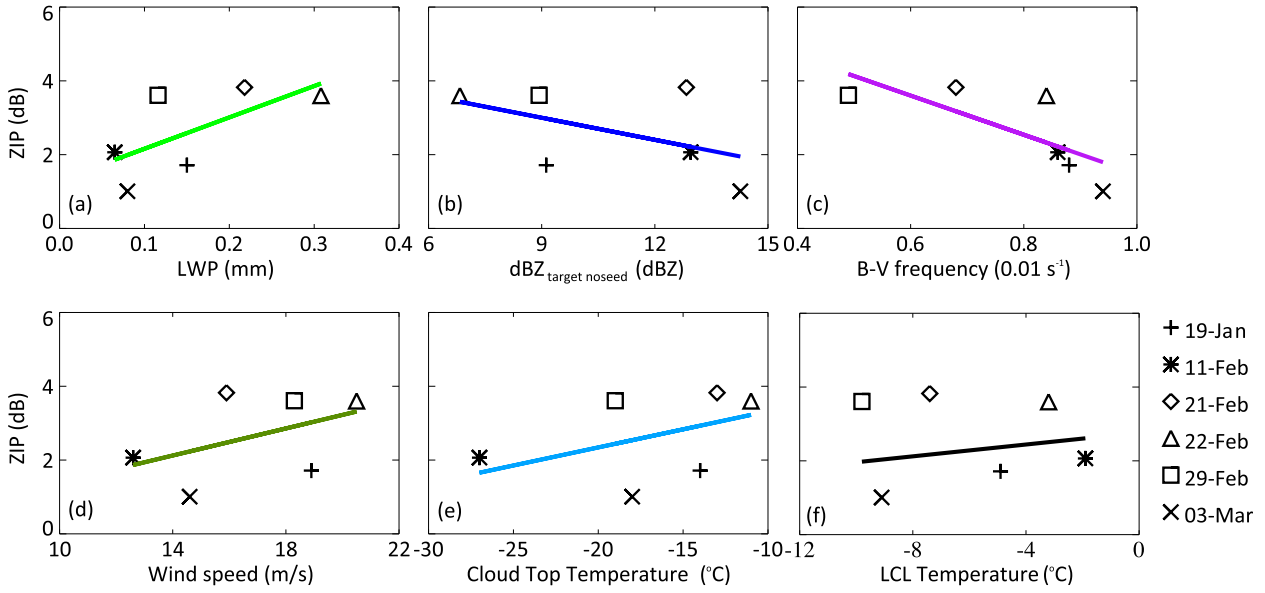


FIG. 18. ZIP as a function of (a) liquid water path, (b) reflectivity of target regions during NOSEED, (c) B–V frequency, (d) wind speed, (e) cloud-top temperature, and (f) cloud-base temperature. The “target” concept here combines “upwind target” and “lee target.” The lines are linear regressions.

control and target regions. This assumption should be reasonable for stratiform precipitation over flat terrain because the decorrelation distance of such precipitation (or  $Z$ ) is much larger than the distance between control and target regions (e.g., Lee et al. 2009). Near mountains, however, subtle changes in stability or wind may change properties of orographic waves, low-level ascent, and lee subsidence (e.g., Durran 1986), and thus the spatial autocorrelation between foothills and mountain crest may be low. The reflectivity profile responds to changes in orographic flow; therefore we examine changes in echo-top height for various  $Z$  thresholds (Fig. 19). A column that does not reach a given threshold  $Z$  (e.g., 10 dBZ) at any level is not included in the count. Thresholds range from 0 (which is close to the DOW echo top and in most cases to cloud top) to 20 dBZ, whose height is close to the surface as  $Z$  typically increases toward the terrain (Fig. 13) because of low-level snow growth. Only those pixels with sufficiently strong echoes are included in the average.

The echo top decreased considerably from NOSEED to SEED in the control area (Fig. 19a). The echo-top heights for all other thresholds decreased there as well, implying that the near-surface  $Z$  (and thus precipitation rate) decreased, consistent with Fig. 13c. Echo-top distributions (not shown) reveal a bimodal distribution. This distribution changes over time, with fewer high tops and more shallow tops during SEED than during NOSEED. In the upwind target area, the

echo top decreased only slightly. The evolution of echo tops from NOSEED to SEED is very different between Fig. 19a and Fig. 19b, likely largely due to changes in orographic flow and thus orographic precipitation. Thus ZIP may be affected also by natural changes in the orographic flow, as is obvious also from the upper portion of the ZIP profiles (Fig. 17). The upper-level changes in the ZIP profiles and the differences in echo-top changes (at low threshold  $Z$  values) probably are all natural. The low-level ZIP values and the slightly higher 11–20-dBZ echo-top heights in the target region are possibly due to AgI seeding. The transition height is not clear, but in general the impact of ground-based seeding in stratiform clouds should be limited to the well-mixed PBL. The echo-height persistency in the upwind target region suggests that the precipitation vertical structure hardly changed from NOSEED to SEED, and therefore a single difference (SEED – NOSEED in target region) may be more representative of the seeding impact than the ZIP. This difference is just ~1 dBZ at low levels (Fig. 13f), which is less than the low-level ZIP (2.8 dBZ). The correlations between ZIP and the several environmental factors (LWP, temperature, wind speed, stability, and snow rate) may also include natural orographic flow changes, because natural orographic precipitation correlates with these factors in general. For example, a warmer environment, more LWC, and stronger wind can increase natural orographic precipitation, as has been shown by modeling studies (e.g., Colle 2004).

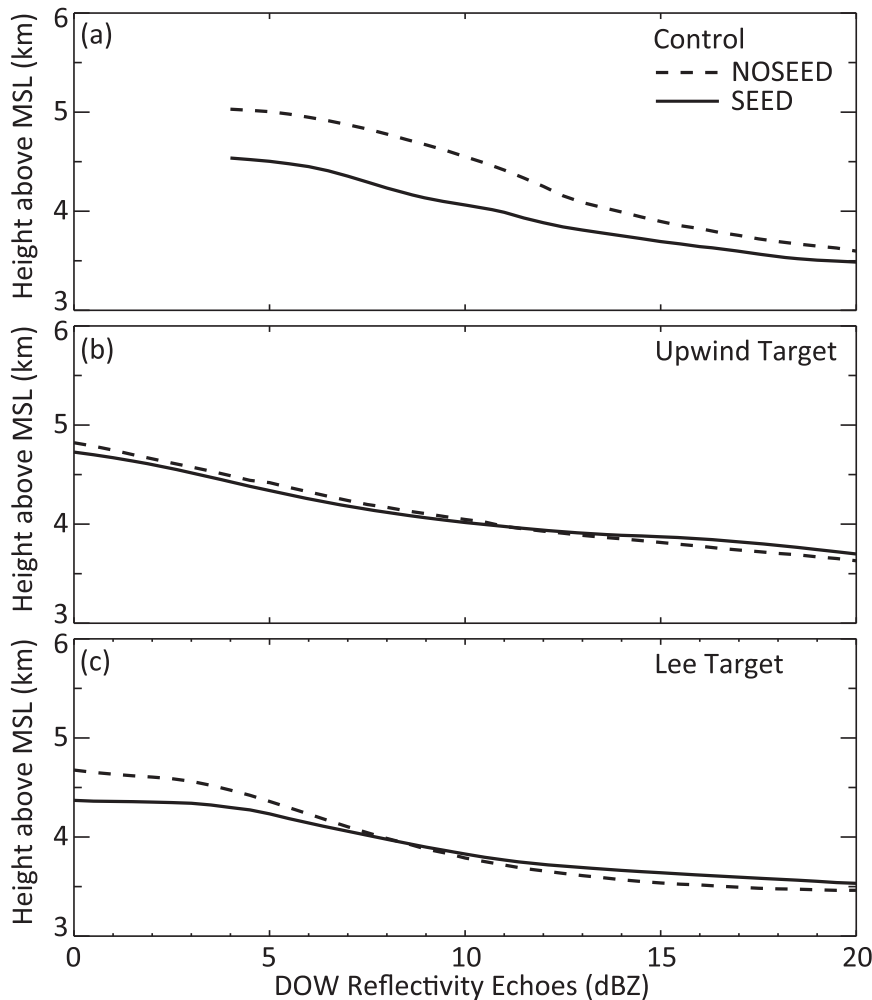


FIG. 19. The mean ceiling of different DOW reflectivity echoes for (a) control, (b) upwind target, and (c) lee target areas during NOSEED and SEED periods, for all six cases.

## 6. Discussion

This study shows that an X-band dual-polarization radar can be a powerful tool to examine the impact of glaciogenic seeding on cloud microphysical processes. The results of this paper corroborate other recent studies (summarized in the introduction) that ground-based AgI seeding can influence snow growth in winter orographic stratiform clouds. This study also highlights the fairly weak seeding signal and also the importance of natural trends, which may not be the same in the control and target regions and may overwhelm the results. The preponderance of evidence—from transects of  $Z$ ,  $ZDR$ , and  $\rho_{HV}$ ; profiles and maps of  $Z$ ; profiles of  $ZDR$ ; displays of  $ZDR$  versus  $Z$ ; and snow photography—suggests that AgI seeding increases snowfall rate in the sampled mostly stratiform orographic clouds, especially through an increased concentration of dendritic ice crystals.

It is clear that the changes can be entirely natural, as trends in the control area do not need to be the same as in the target area, even if they are similar (Fig. 12). In fact DOW data show echo top waning in the control area from the NOSEED to SEED period—a change that is not observed in the target area. Therefore, as one cannot fully capture the natural trend of precipitation, the attribution needs to be treated with caution, and more observations using radars such as the DOW and WCR, as well as in situ measurements and numerical simulations, are needed to better characterize the seeding signature and conditions that are most suitable for seeding. Suggested improvements in the experimental design include the use of a lateral control area (over the mountain range but to the side of the AgI plumes), because it may be more representative, and the targeting of simpler clouds first, such as supercooled stratus clouds that are decoupled from the surface.

Nevertheless, this study is a useful contribution to the body of observational weather-modification literature, because it is the first to examine X-band radar reflectivity changes across a mountain range and the first to explore changes in dual-polarization variables in the context of glaciogenic cloud seeding.

## 7. Conclusions

The impact of ground-based glaciogenic seeding on snow growth in winter orographic mostly stratiform clouds is analyzed using a scanning X-band dual-polarization DOW radar. Data are collected from all suitable IOPs in the ASCII-12 campaign conducted over the Sierra Madre in southern Wyoming. This paper presents one case study (11 February 2012) and a composite analysis of the six IOPs with mostly stratiform precipitation and steady conditions. To examine the seeding impact, three study areas are designated (one control region and two target regions), and a comparison is made between the measurements from a treated period (SEED) and those from an untreated period (NOSEED), which usually precedes SEED. The main findings are as follows:

- Observations from the case study (11 February)—profiles and maps of  $Z$  and ZDR, displays of ZDR versus  $Z$ , and snow photography on the ground—indicate the following in the close-fetch upwind target region during seeding:  $Z$  and ZDR increases at low levels, a ZDR increase for most  $Z$  values, and mostly unrimed snowflakes and large dendritic ice crystals on the ground. These changes happened notwithstanding a (natural) decrease in cloud-top height across the region during seeding. Any seeding signature is weaker and shallower in the more distant ( $>18$  km) lee target region.
- Changes in dual-polarization variables in the case study suggest a relative increase in concentration of dendrites and plates and suggest snow growth by vapor diffusion rather than by droplet accretion during seeding. Low-level ZDR values tend to be larger, which suggests fewer rimed particles and more dendritic ice crystals during seeding, as confirmed by crystal photography on the ground.
- The composite analysis of six cases reveals an increase in low-level  $Z$  in the target region (relative to the control region) during SEED. Thus the variable ZIP, a double-difference variable that is proportional to the double-ratio precipitation change (SEED vs NOSEED temporal change in the target region vs the same in the control region), is positive in all cases for the upwind target region. The ZIP magnitude is 2–3 dB on average

near the surface, which implies a substantial ( $\sim 50\%$ ) increase in precipitation rate.

- The composite ZIP profile is positive also toward the cloud top, because the radar echo-top height decreased considerably in the control region (between NOSEED and SEED) while it remained roughly unchanged in the target region. This result suggests that natural changes (differences in echo-top height evolution between the control and target regions) contributed to the observed differences in the SEED versus NOSEED change in low-level  $Z$  between the control and target regions, rather than AgI seeding alone.
- There is some suggestion that the seeding efficacy increases with cloud LWP, cloud-base temperature, cloud-top temperature, and wind speed and decreases with stability and snowfall rate, at least within the narrow observed parameter space. These findings, while consistent with expectations from the literature, are not robust, however, because they are based on just six cases.

*Acknowledgments.* The ASCII campaign, including the operation of the DOW, was funded by National Science Foundation Grant AGS-1058426. This work also received funding from the Wyoming Water Development Commission and the U.S. Geological Survey, under the auspices of the University of Wyoming Water Research Program. The operation of the AgI generators and microwave radiometer was supported by the Wyoming Weather Modification Pilot Project, which is funded by the State of Wyoming. The dedication of the DOW crew under harsh weather conditions at Battle Pass during ASCII is much appreciated. Kyoko Ikeda kindly provided the snow gauge data for 11 February 2012. This work benefitted from discussions with and assistance provided by Joshua Aikins of the University of Colorado and from the insights of three anonymous reviewers.

## REFERENCES

- Boe, B. A., J. A. Heimbach, T. W. Krauss, L. Xue, X. Chu, and J. T. McPartland, 2014: The dispersion of silver iodide particles from ground-based generators over complex terrain. Part I: Observations with acoustic ice nucleus counters. *J. Appl. Meteor. Climatol.*, **53**, 1325–1341, doi:10.1175/JAMC-D-13-0240.1.
- Boudala, F. S., G. A. Isaac, S. G. Cober, and Q. Fu, 2004: Liquid fraction in stratiform mixed-phase clouds from in situ observations. *Quart. J. Roy. Meteor. Soc.*, **130**, 2919–2931, doi:10.1256/qj.03.153.
- Breed, D., R. Rasmussen, C. Weeks, B. Boe, and T. Deshler, 2014: Evaluating winter orographic cloud seeding: Design of the Wyoming Weather Modification Pilot Project (WWMPP). *J. Appl. Meteor. Climatol.*, **53**, 282–299, doi:10.1175/JAMC-D-13-0128.1.

- Bruintjes, R. T., 1999: A review of cloud seeding experiments to enhance precipitation and some new prospects. *Bull. Amer. Meteor. Soc.*, **80**, 805–820, doi:10.1175/1520-0477(1999)080<0805:AROCSE>2.0.CO;2.
- Chu, X., L. Xue, B. Geerts, R. Rasmussen, and D. Breed, 2014: A case study of radar observations and WRF LES simulations of the impact of ground-based glaciogenic seeding on orographic clouds and precipitation. Part I: Observations and model validations. *J. Appl. Meteor. Climatol.*, **53**, 2264–2286, doi:10.1175/JAMC-D-14-0017.1.
- Colle, B. A., 2004: Sensitivity of orographic precipitation to changing ambient conditions and terrain geometries: An idealized modeling perspective. *J. Atmos. Sci.*, **61**, 588–606, doi:10.1175/1520-0469(2004)061<0588:SOOPTC>2.0.CO;2.
- Cunningham, J. G., and S. E. Yuter, 2014: Instability characteristics of radar-derived mesoscale organization modes within cool-season precipitation near Portland, Oregon. *Mon. Wea. Rev.*, **142**, 1738–1757, doi:10.1175/MWR-D-13-00133.1.
- Dennis, A. S., A. Koscielski, D. E. Cain, J. H. Hirsch, and P. L. Smith, 1975: Analysis of radar observations of a randomized cloud seeding experiment. *J. Appl. Meteor.*, **14**, 897–908, doi:10.1175/1520-0450(1975)014<0897:AOROOA>2.0.CO;2.
- DeMott, P. J., 1997: Report to North Dakota Atmospheric Resource Board and Weather Modification Incorporated on tests of the ice nucleating ability of aerosols produced by the Lohse Airborne Generator. Colorado State University Dept. of Atmospheric Science Tech. Rep., 38 pp.
- Deshler, T., D. W. Reynolds, and A. W. Huggins, 1990: Physical response of winter orographic clouds over the Sierra Nevada to airborne seeding using dry ice or silver iodide. *J. Appl. Meteor.*, **29**, 288–330, doi:10.1175/1520-0450(1990)029<0288:PROWOC>2.0.CO;2.
- Durran, D. R., 1986: Another look at downslope windstorms. Part I: The development of analogs to supercritical flow in an infinitely deep, continuously stratified fluid. *J. Atmos. Sci.*, **43**, 2527–2543, doi:10.1175/1520-0469(1986)043<2527:ALADWP>2.0.CO;2.
- Gabriel, K. R., 1999: Ratio statistics for randomized experiments in precipitation stimulation. *J. Appl. Meteor.*, **38**, 290–301, doi:10.1175/1520-0450(1999)038<0290:RSFREI>2.0.CO;2.
- Gagin, A., 1986: Evaluation of “static” and “dynamic” seeding concepts through analyses of Israeli II and FACE-2 experiments. *Precipitation Enhancement—A Scientific Challenge*, Meteor. Monogr., No. 43, Amer. Meteor. Soc., 63–76.
- , D. Rosenfeld, W. L. Woodley, and R. E. Lopez, 1986: Results of seeding for dynamic effect on rain-cell properties in FACE-2. *J. Climate Appl. Meteor.*, **25**, 3–13, doi:10.1175/1520-0450(1986)025<0003:ROSFDE>2.0.CO;2.
- Geerts, B., Q. Miao, Y. Yang, R. Rasmussen, and D. Breed, 2010: An airborne profiling radar study of the impact of glaciogenic cloud seeding on snowfall from winter orographic clouds. *J. Atmos. Sci.*, **67**, 3286–3301, doi:10.1175/2010JAS3496.1.
- , —, and —, 2011: Boundary-layer turbulence and orographic precipitation growth in cold clouds: Evidence from profiling airborne radar data. *J. Atmos. Sci.*, **68**, 2344–2365, doi:10.1175/JAS-D-10-05009.1.
- , and Coauthors, 2013: The AgI Seeding Cloud Impact Investigation (ASCI) campaign 2012: Overview and preliminary results. *J. Wea. Modif.*, **45**, 24–43.
- , Y. Yang, R. Rasmussen, S. Haimov, and B. Pokharel, 2015: Snow growth and transport patterns in orographic storms as estimated from airborne vertical-plane dual-Doppler radar data. *Mon. Wea. Rev.*, **143**, 644–665, doi:10.1175/MWR-D-14-00199.1.
- Gourley, J. J., P. Tabary, and J. P. D. Chatelet, 2007: A fuzzy logic algorithm for the separation of precipitating from non-precipitating echoes using polarimetric radar observations. *J. Atmos. Oceanic Technol.*, **24**, 1439–1451, doi:10.1175/JTECH2035.1.
- Grant, L. O., and R. E. Elliott, 1974: The cloud seeding temperature window. *J. Appl. Meteor.*, **13**, 355–363, doi:10.1175/1520-0450(1974)013<0355:TCSTW>2.0.CO;2.
- Hobbs, P. V., J. H. Lyons, J. D. Locatelli, K. R. Biswas, L. F. Radke, R. R. Weiss, and A. L. Rangno, 1981: Radar detection of cloud-seeding effects. *Science*, **213**, 1250–1252, doi:10.1126/science.213.4513.1250.
- Holroyd, E. W., J. T. McPartland, and A. B. Super, 1988: Observation of silver iodide plumes over the Grand Mesa of Colorado. *J. Appl. Meteor.*, **27**, 1125–1144, doi:10.1175/1520-0450(1988)027<1125:OOSIPO>2.0.CO;2.
- , J. A. Heimbach, and A. B. Super, 1995: Observations and model simulation of AgI seeding within a winter storm over Utah’s Wasatch Plateau. *J. Wea. Modif.*, **27**, 35–56.
- Houze, R. A., Jr., 1993: *Cloud Dynamics*. Academic Press, 573 pp.
- Huggins, A. W., 1995: Mobile microwave radiometer observations: Spatial characteristics of supercooled cloud water and cloud seeding implications. *J. Appl. Meteor.*, **34**, 432–446, doi:10.1175/1520-0450-34.2.432.
- , 2007: Another wintertime cloud seeding case study with strong evidence of seeding effects. *J. Wea. Modif.*, **39**, 9–36.
- Jing, X., and B. Geerts, 2015: Dual-polarization radar data analysis of the impact of ground-based glaciogenic seeding on winter orographic clouds. Part II: Convective clouds. *J. Appl. Meteor. Climatol.*, doi:10.1175/JAMC-D-15-0056.1, in press.
- Kucera, P. A., A. Theisen, and D. Langerud, 2008: Polarimetric Cloud Analysis and Seeding Test (POLCAST). *J. Wea. Modif.*, **40**, 64–76.
- Langmuir, I., 1950: Control of precipitation from cumulus clouds by various seeding techniques. *Science*, **112**, 35–41, doi:10.1126/science.112.2898.35.
- Lee, C. K., G. W. Lee, I. Zawadzki, and K.-E. Kim, 2009: A preliminary analysis of spatial variability of raindrop size distributions during stratiform rain events. *J. Appl. Meteor. Climatol.*, **48**, 270–283, doi:10.1175/2008JAMC1877.1.
- Manton, M. J., and L. Warren, 2011: A confirmatory snowfall enhancement project in the Snowy Mountains of Australia. Part II: Primary and associated analyses. *J. Appl. Meteor. Climatol.*, **50**, 1448–1458, doi:10.1175/2011JAMC2660.1.
- Markowski, P., and Y. Richardson, 2010: *Mesoscale Meteorology in Midlatitudes*. Wiley-Blackwell, 407 pp.
- Matrosov, S. Y., C. Campbell, D. Kingmill, and E. Sukovich, 2009: Assessing snowfall rates from X-band radar reflectivity measurements. *J. Atmos. Oceanic Technol.*, **26**, 2324–2339, doi:10.1175/2009JTECHA1238.1.
- Miao, Q., and B. Geerts, 2013: Airborne measurements of the impact of ground-based glaciogenic cloud seeding on orographic precipitation. *Adv. Atmos. Sci.*, **30**, 1025–1038, doi:10.1007/s00376-012-2128-2.
- Morrison, A. E., S. T. Siems, and M. J. Manton, 2013: On a natural environment for glaciogenic cloud seeding. *J. Appl. Meteor. Climatol.*, **52**, 1097–1104, doi:10.1175/JAMC-D-12-0108.1.
- National Research Council, 2003: *Critical Issues in Weather Modification Research*. National Academies Press, 123 pp.

- Oye, R., C. Mueller, and S. Smith, 1995: Software for radar translation, visualization, editing, and interpolation. Preprints, *27th Conf. on Radar Meteorology*, Vail, CO, Amer. Meteor. Soc., 359–361.
- Plummer, D. M., S. Göke, R. M. Rauber, and L. D. Girolamo, 2010: Discrimination of mixed- versus ice-phase clouds using dual-polarization radar with application to detection of aircraft icing regions. *J. Appl. Meteor. Climatol.*, **49**, 920–936, doi:10.1175/2009JAMC2267.1.
- Pokharel, B., B. Geerts, and X. Jing, 2014a: The impact of ground-based glaciogenic seeding on orographic clouds and precipitation: A multi-sensor case study. *J. Appl. Meteor. Climatol.*, **53**, 890–909, doi:10.1175/JAMC-D-13-0290.1.
- , and Coauthors, 2014b: The impact of ground-based glaciogenic seeding on clouds and precipitation over mountains: A multi-sensor case study of shallow precipitating orographic cumuli. *Atmos. Res.*, **147–148**, 162–182, doi:10.1016/j.atmosres.2014.05.014.
- Que, M., M. Galletti, J. Verlinde, and E. E. Clothiaux, 2013: Ice crystals in Arctic mixed-phase clouds observed by an X-band polarimetric radar. Presentation, *2013 ASR Fall Working Groups Meeting*, Rockville, MD, U.S. Dept. of Energy Atmospheric System Research, 23 pp. [Available online at <http://asr.science.energy.gov/meetings/fall-working-groups/2013/presentations/oue.pdf>.]
- Ritzman, J. M., 2013: Estimates of the fraction of precipitation seedable under application of the Wyoming Weather Modification Pilot Project seeding criteria. M.S. thesis, Dept. of Atmospheric Science, University of Wyoming, 96 pp.
- Rosenfeld, D., and W. L. Woodley, 1989: Effects of cloud seeding in west Texas. *J. Appl. Meteor.*, **28**, 1050–1080, doi:10.1175/1520-0450(1989)028<1050:EOCSIW>2.0.CO;2.
- Rutledge, S. A., and P. V. Hobbs, 1983: The mesoscale and microscale structure and organization of clouds and precipitation in midlatitude cyclones. VIII: A model for the “seeder-feeder” process in warm-frontal rainbands. *J. Atmos. Sci.*, **40**, 1185–1206, doi:10.1175/1520-0469(1983)040<1185:TMAMSA>2.0.CO;2.
- Silverman, B. A., 2001: A critical assessment of glaciogenic seeding of convective clouds for rainfall enhancement. *Bull. Amer. Meteor. Soc.*, **82**, 903–921, doi:10.1175/1520-0477(2001)082<0903:ACAOGS>2.3.CO;2.
- Simpson, J., and W. L. Woodley, 1971: Seeding cumulus in Florida: New 1970 results. *Science*, **172**, 117–126, doi:10.1126/science.172.3979.117.
- Smith, E. J., 1949: Experiments in seeding cumuliform cloud layers with dry ice. *Aust. J. Sci. Res.*, **2**, 78–91.
- Super, A. B., 1974: Silver iodide plume characteristics over the Bridger Mountain Range, Montana. *J. Appl. Meteor.*, **13**, 62–70, doi:10.1175/1520-0450(1974)013<0062:SIPCOT>2.0.CO;2.
- , 1999: Summary of the NOAA/Utah Atmospheric Modification Program: 1990–1998. *J. Wea. Modif.*, **31**, 51–75.
- , and B. A. Boe, 1988: Microphysical effects of wintertime cloud seeding with silver iodide over the Rocky Mountains. Part III: Observations over the Grand Mesa, Colorado. *J. Appl. Meteor.*, **27**, 1166–1182, doi:10.1175/1520-0450(1988)027<1166:MEOWCS>2.0.CO;2.
- , and J. A. Heimbach, 1988: Microphysical effects of wintertime cloud seeding with silver iodide over the Rocky Mountains. Part II: Observations over the Bridger Range, Montana. *J. Appl. Meteor.*, **27**, 1152–1165, doi:10.1175/1520-0450(1988)027<1152:MEOWCS>2.0.CO;2.
- Thompson, E. J., S. A. Rutledge, B. Dolan, V. Chandrasekar, and B. L. Cheong, 2014: A dual-polarization radar hydrometeor classification algorithm for winter precipitation. *J. Atmos. Oceanic Technol.*, **31**, 1457–1481, doi:10.1175/JTECH-D-13-00119.1.
- Vali, G., D. Leon, and J. R. Snider, 2012: Ground-layer snow clouds. *Quart. J. Roy. Meteor. Soc.*, **138**, 1507–1525, doi:10.1002/qj.1882.
- Vivekanandan, J., V. N. Bringi, M. Hagen, and P. Meischner, 1994: Polarimetric radar studies of atmospheric ice particles. *IEEE Trans. Geosci. Remote Sens.*, **32**, 1–10, doi:10.1109/36.285183.
- , S. M. Ellis, R. Oye, D. S. Zrnich, A. V. Ryzhkov, and J. Straka, 1999: Cloud microphysics retrieval using S-band dual-polarization radar measurements. *Bull. Amer. Meteor. Soc.*, **80**, 381–388, doi:10.1175/1520-0477(1999)080<0381:CMRUSB>2.0.CO;2.
- Vonnegut, B., and H. Chessin, 1971: Ice nucleation by coprecipitated silver iodide and silver bromide. *Science*, **174**, 945–946, doi:10.1126/science.174.4012.945.
- Xue, L., and Coauthors, 2013a: AgI cloud seeding effects as seen in WRF simulations. Part I: Model description and idealized 2D sensitivity tests. *J. Appl. Meteor. Climatol.*, **52**, 1433–1457, doi:10.1175/JAMC-D-12-0148.1.
- , S. Tessendorf, E. Nelson, R. Rasmussen, D. Breed, S. Parkinson, P. Holbrook, and D. Blestrud, 2013b: AgI cloud seeding effects as seen in WRF simulations. Part II: 3D real case simulations and sensitivity tests. *J. Appl. Meteor. Climatol.*, **52**, 1458–1476, doi:10.1175/JAMC-D-12-0149.1.
- , X. Chu, R. Rasmussen, D. Breed, B. Boe, and B. Geerts, 2014: The dispersion of silver iodide particles from ground-based generators over complex terrain. Part II: WRF large-eddy simulations versus observations. *J. Appl. Meteor. Climatol.*, **53**, 1342–1361, doi:10.1175/JAMC-D-13-0241.1.
- , —, —, —, and B. Geerts, 2015: A case study of radar observations and WRF LES simulations of the impact of ground-based glaciogenic seeding on orographic clouds and precipitation. Part II: AgI dispersion and seeding signals simulated by WRF. *J. Appl. Meteor. Climatol.*, submitted.
- Yuter, S. E., and R. A. Houze Jr., 1995: Three-dimensional kinematic and microphysical evolution of Florida cumulonimbus. Part II: Frequency distributions of vertical velocity, reflectivity, and differential reflectivity. *Mon. Wea. Rev.*, **123**, 1941–1963, doi:10.1175/1520-0493(1995)123<1941:TDKAME>2.0.CO;2.